RESEARCH ARTICLE

Basin Research   EAGE WILEY

Location, extent, and magnitude of dynamic topography in the Late Cretaceous Cordilleran Foreland Basin, USA: New insights from 3D flexural backstripping

Zhiyang Li[1,2] [iD] | Jennifer Aschoff[1]

[1]Department of Geological Sciences, University of Alaska, Anchorage, Alaska, USA

[2]School of Engineering, Texas A&M International University, Laredo, Texas, USA

Correspondence
Zhiyang Li, School of Engineering, Texas A&M International University, Laredo, TX 78041, USA.
Email: zhiyang.li@tamiu.edu

Abstract

Mantle-induced dynamic topography (i.e., subsidence and uplift) has been increasingly recognized as an important process in foreland basin development. However, characterizing and distinguishing the effects (i.e., location, extent and magnitude) of dynamic topography in ancient foreland basins remains challenging because the spatio-temporal footprint of dynamic topography and flexural topography (i.e., generated by topographic loading) can overlap. This study employs 3D flexural backstripping of Upper Cretaceous strata in the central part of the North American Cordilleran foreland basin (CFB) to better quantify the effects of dynamic topography. The extensive stratigraphic database and good age control of the CFB permit the regional application of 3D flexural backstripping in this basin for the first time. Dynamic topography started to influence the development of the CFB during the late Turonian to middle Campanian (90.2–80.2 Ma) and became the dominant subsidence mechanism during the middle to late Campanian (80.2–74.6 Ma). The area influenced by >100 m dynamic subsidence is approximately 400 by 500 km, within which significant (>200 m) dynamic subsidence occurs in an irregular-shaped (i.e., lunate) subregion. The maximum magnitude of dynamic subsidence is 300 ± 100 m based on the 80.2–74.6 Ma tectonic subsidence maps. With the maximum magnitude of dynamic uplift being constrained to be 200–300 m, the gross amount of dynamic topography in the Late Cretaceous CFB is 500–600 m. Although the location of dynamic subsidence revealed by tectonic subsidence maps is generally consistent with isopach map trends, tectonic subsidence maps developed through 3D flexural backstripping provide more accurate constraints of the areal extent, magnitude and rate of dynamic topography (as well as flexural topography) in the CFB through the Late Cretaceous. This improved understanding of dynamic topography in the CFB is critical for refining current geodynamic models of foreland basins and understanding the surface expression of mantle processes.

KEYWORDS

3D flexural backstripping, Cordilleran foreland basin, dynamic topography, Late Cretaceous

—WILEY—

1 | INTRODUCTION

Foreland basins, which form as elongate troughs parallel to fold-and-thrust belts along convergent plate boundaries, ultimately owe their existence to flexure of the lithosphere caused by loading (Allen & Allen, 2013; Watts, 2001). At present, most foreland basin models emphasize the importance of flexural subsidence caused by supracrustal loadings, such as orogenically thickened crust and the sediment and water filling in the basin (Angevine et al., 1990; DeCelles, 2012). A generic foreland basin formed dominantly by flexural subsidence consists of four discrete depozones: wedge top, foredeep, forebulge and backbulge (DeCelles & Giles, 1996). The width and geometry of a foreland basin generated dominantly by the loading of a thrust sheet are subject mainly to the flexural rigidity of the lithosphere and the size of the orogenic load (Allen & Allen, 2013; Beaumont, 1981;DeCelles, 2012; Jordan, 1981). For a given load, the basin developed on a stiffer lithosphere (higher rigidity) would be characterized by less subsidence and the forebulge located at a greater distance from the thrust load (DeCelles, 2012; Jordan, 1981).

In foreland basins, particularly those formed in retroarc settings, the dynamic coupling between the subducting oceanic plate and the overlying plate is another important process controlling the basin development (Burgess et al., 1997; Gurnis, 1992; Mitrovica et al., 1989). The subsidence and uplift of the lithosphere caused by the dynamic coupling are collectively termed dynamic topography (Mitrovica et al., 1989; Richards & Hager, 1984). For instance, the downward drag associated with the viscous mantle corner flow above a subducting plate can result in dynamic subsidence (Burgess et al., 1997; Dávila & Lithgow-Bertelloni, 2015). Due to the large-scale mantle flow, the effect of subcrustal loading can translate to much larger distances (ca. 1000 km) from the subduction zone and lead to subsidence in areas farther away (>400 km) from the fold-thrust belt (Burgess & Moresi, 1999; Catuneanu et al., 1997; Gurnis, 1992; Mitrovica et al., 1989). Dynamic uplift may result from slab flattening when an aseismic ridge with thickened crust on the oceanic lithosphere is subducted, under which condition the negative buoyancy of the subducting plate and the dynamic coupling between the mantle and the lithosphere are greatly reduced (Dávila & Lithgow-Bertelloni, 2015; Heller & Liu, 2016). Unlike the flexural subsidence generated by a topographic load, the effects (e.g., location and magnitude of subsidence/uplift) of mantle-induced dynamic topography remain less well understood, largely due to the complex heterogeneity in the Earth's mantle (Flament et al., 2013; Koppers et al., 2021; Liu, 2015; Liu et al., 2008; Richards & Hager, 1984).

Highlights

- 3D flexural backstripping has been applied to the Cordilleran foreland basin (CFB) for the first time.
- Dynamic topography started to influence the CFB in 90–80 Ma and became the dominant subsidence mechanism in 80–75 Ma.
- The gross dynamic topography (i.e., subsidence and uplift) in the Late Cretaceous CFB is 500–600 m.
- The effects (e.g., location, extent, and rate) of dynamic topography are transitory.
- 3D flexural backstripping more accurately depicts tectonic subsidence and uplift trend than isopach maps.

Although dynamic topography has been increasingly recognized as an important subsidence mechanism in retroarc foreland basins (Chang & Liu, 2020; Dávila & Lithgow-Bertelloni, 2015; DeCelles, 2012; Lazauskien et al., 2002; Li & Aschoff, 2022a; Liu et al., 2014; Painter & Carrapa, 2013; Shephard et al., 2010; Tufano & Pietras, 2017), clear discrimination between traditionally recognized flexural subsidence and dynamic subsidence remains challenging. Considering the North American Cordilleran foreland basin (CFB) formed by subduction of the oceanic Farallon plate beneath the North American plate, it has long been recognized that the combined effects of flexural loading and eustasy are not enough to account for the kilometre-thick sedimentary deposits in the interior of the basin (>300 km away from the thrust belt; Bond, 1976; Cross & Pilger, 1978). The additional subsidence needed to explain the stratal thickness and the eastward shift in depocenter has been attributed to dynamic subsidence caused by the cold oceanic lithosphere being subducted at a shallow angle below the overlying continental lithosphere (Gurnis, 1992; Heller & Liu, 2016; Liu et al., 2011; Mitrovica et al., 1989; Painter & Carrapa, 2013). Nevertheless, the spatio-temporal effects (e.g., location, extent and magnitude) of dynamic topography in the CFB remains poorly constrained. Although geodynamic modelling can shed some light on the location and amount of dynamic subsidence (and uplift) in such convergent systems, results from different models inevitably depart in detail due to many inherent uncertainties in solid Earth parameters (e.g., the subduction geometry, age of the subducted oceanic crust, rheology of the mantle; Liu & Gurnis, 2010; Humphreys et al., 2015; Koppers et al., 2021).

Many studies have attempted to constrain the effects of dynamic topography (particularly dynamic subsidence) recorded in the stratigraphic record of CFB (Cross & Pilger, 1978; Li & Aschoff, 2022a; Liu et al., 2011; Painter & Carrapa, 2013). One of the common methods to examine the effects of different subsidence mechanisms is based on isopach maps (stratal thickness). Cross and Pilger (1978) first attributed the broad depocenter in southern Wyoming, central and northern Colorado and eastern Utah revealed on the Campanian to Maastrichtian isopach map to subcrustal loading or cooling associated with the shallowing subduction of the oceanic lithosphere. Isopach maps developed from subsequent studies generally agree with the presence and location of this broad depocenter during this time (Roberts & Kirschbaum, 1995), and the distance between the fold-thrust belt and the depocenter serves as one of the most important criteria to distinguish dynamic subsidence (long-wavelength) from flexural subsidence (short-wavelength; Burgess & Moresi, 1999; Liu & Nummedal, 2004; Spasojevic et al., 2009). More recent isopach maps with more control points indicate that dynamic subsidence became the dominant subsidence mechanism in the CFB at ca. 80 Ma (Li & Aschoff, 2022a; Painter & Carrapa, 2013). Although isopach maps can portray the long-term tectonic subsidence pattern, and thus help constrain the location of dynamic subsidence, they cannot directly reveal the magnitude of different tectonic subsidence mechanisms (regardless of the origin). This is because stratal thickness represents the compacted thickness of sediments that once filled the accommodation generated by the combined tectonic subsidence, eustasy and the weight of the infilling sediments and water (Angevine et al., 1990; Sclater & Christie, 1980; Steckler & Watts, 1978).

To extract tectonic subsidence from the stratigraphic record, the effects of compaction, sediment loading, eustatic changes and water depth need to be removed through a process termed backstripping (Allen & Allen, 2013; Angevine et al., 1990; Sclater & Christie, 1980; Steckler & Watts, 1978). A number of studies have applied the 1D backstripping technique based on local (Airy) isostasy (assuming the lithosphere has no lateral strength) using geophysical well logs to compare the subsidence trend across the CFB (Heller et al., 1986; Heller & Liu, 2016; Martinson et al., 1998). Although 1D backstripping is a relatively simple process and requires far less data (i.e., 1D stratigraphic sections or geophysical well logs), it is not as accurate for interpreting basin subsidence as flexural backstripping. This is especially the case for highly asymmetrical foreland basins like the CFB, in which the flexural effects of the wedge-shaped sediment fill can be too significant to be ignored (Chang & Liu, 2019; Pang, 1995). Indeed, a few previous studies have applied 2D flexural backstripping (based on 2D stratigraphic cross sections) to investigate the subsidence history of the CFB. Although these studies all point out that the tectonic subsidence in the CFB likely is the combined result of flexural subsidence and dynamic subsidence (Liu et al., 2011; Liu et al., 2014; Pang & Nummedal, 1995), the magnitude of dynamic subsidence calculated through 2D flexural backstripping is still not accurate enough because the likely variation in sediment thickness (i.e., flexure caused by sediment loading) off the cross-sections was not considered. A more accurate approach to constrain the magnitude of dynamic subsidence is 3D flexural backstripping, which, to the authors' knowledge, has not yet been implemented in the CFB.

To better understand the tectonic subsidence history of the CFB, the 3D flexural backstripping technique was applied to the Upper Cretaceous strata in the central part of the CFB (Wyoming, Utah, Colorado and New Mexico). This stratigraphic interval and geographic area were chosen because: (1) dynamic topography is documented to have played a significant role in these areas during the Late Cretaceous (Aschoff & Steel, 2011; Heller & Liu, 2016; Li & Aschoff, 2022a; Liu et al., 2011; Liu et al., 2014; Liu & Gurnis, 2010) and (2) the extensive outcrop to subsurface dataset here allows the development of a series of high-resolution isopach maps (Li & Aschoff, 2022a), which are an important prerequisite for 3D flexural backstripping (Pang, 1995). As the first 3D flexural backstripping study in the CFB, this study provides a quantitative characterization of the location, extent, magnitude and rate of dynamic topography through time (including both subsidence and uplift) in the CFB, which is critical to constrain and refine the current geodynamic model of mantle flows and the resulting dynamic topography in oceanic-continental convergent systems.

2 | GEOLOGIC CONTEXT

The geology of western North America was largely controlled by the subduction of the Farallon plate beneath the North American plate from Jurassic to Paleogene time. The compressive forces associated with plate convergence, combined with conductive heating initiated by subduction, led to crustal thickening in orogenic belts such as the Sevier fold-thrust belt (DeCelles, 2004; Livaccari, 1991). In response to crustal loading, the CFB developed coeval with the folding and thrusting as a broad retroarc foreland basin on the eastern margin of the Sevier fold-thrust belt (Figure 1a; Kauffman, 1985; Kauffman & Caldwell, 1993). Throughout the Late Cretaceous, the Sevier fold-thrust belt propagated irregularly eastward, as did the CFB (DeCelles, 2004; Haque et al., 2020; Liu et al., 2005). In addition to short-wavelength (<300 km) flexural subsidence,
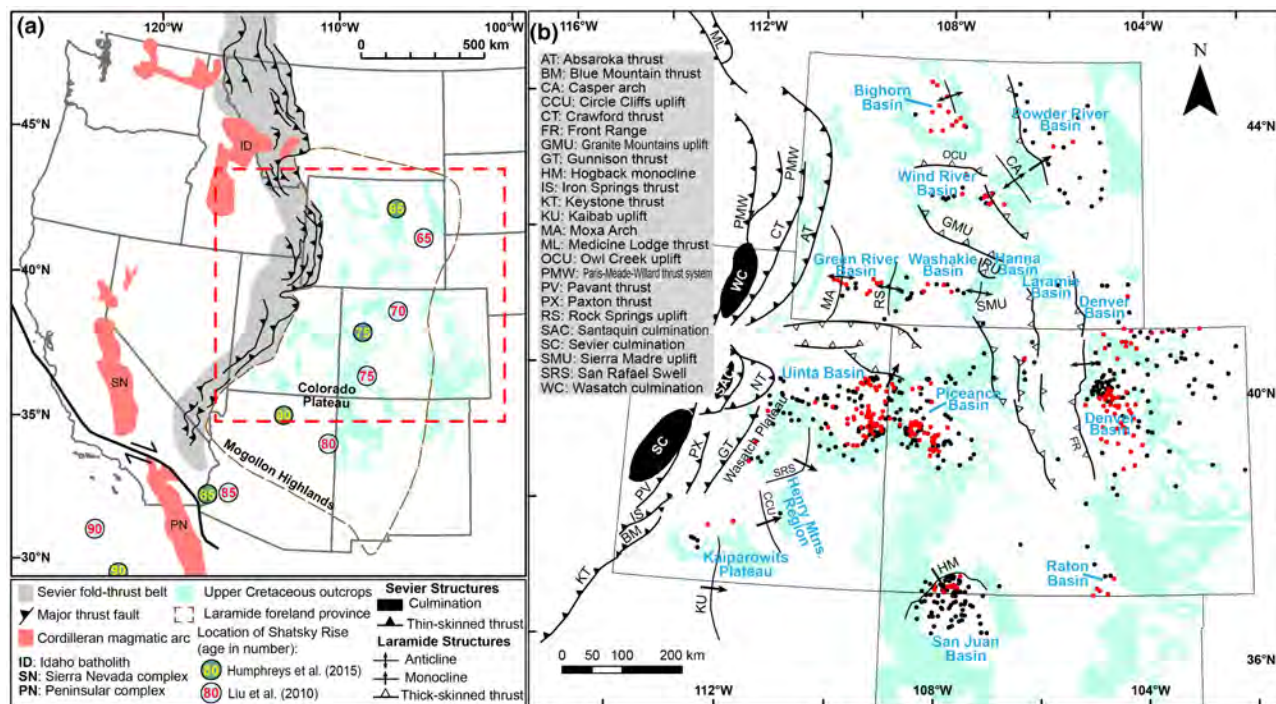
FIGURE 1 (a) Regional index map of the western U.S. including the Sevier fold-thrust belt, Laramide province and Cordilleran magmatic arc (modified from DeCelles, 2004; Yonkee & Weil, 2015). The dashed red box indicates the extent of our study area. Approximate locations of the conjugate Shatsky Rise during 90–65 ma from Liu et al. (2010) and Humphreys et al. (2015) are shown. The legend of different structural features applies to all maps shown in this study. (b) Map of the study area showing the outcrops of Upper Cretaceous strata and multiple basins and regions. The map also shows Sevier (thin-skinned) thrusts (DeCelles, 2004) and Laramide (thick-skinned) structures (Dickinson et al., 1988; Yonkee & Weil, 2015) that were active at different times through the Late Cretaceous. Black and red dots indicate the locations of 627 geophysical well logs in our dataset. Well logs used for decompaction are indicated by red dots.

dynamic subsidence induced by large-scale mantle downwelling associated with the flat subduction of the Farallon slab has been increasingly recognized to play an important role in producing long-wavelength (e.g., >400 km away from the Sevier fold-thrust belt), regional-scale subsidence in the CFB (Chang & Liu, 2019; Heller & Liu, 2016; Leary et al., 2015; Li & Aschoff, 2022a; Painter & Carrapa, 2013).

Late Cretaceous subsidence in the CFB is generally considered to have occurred in three distinct phases. During Cenomanian to Coniacian time, the CFB was characterized by a narrow, deep depocenter adjacent to the Sevier orogenic belt (Cross & Pilger, 1978; DeCelles, 2004; Roberts & Kirschbaum, 1995). Starting in the Santonian, the isopach pattern characteristic of flexural subsidence becomes diffuse (DeCelles, 2004; Roberts & Kirschbaum, 1995). By early Campanian, the depocenter in CFB became broader and migrated away from the thrust front, indicating a greater component of long-wavelength dynamic subsidence, which has been considered to be the result of large-scale mantle downwelling flows associated with the flat subduction of the Farallon slab under the North America (Chang & Liu, 2020; Li & Aschoff, 2022a; Liu et al., 2011; Mitrovica et al., 1989; Painter & Carrapa, 2013). Previous studies have linked

the development of the flat subduction of the Farallon Plate to the subduction of a buoyant oceanic plateau—the conjugate Shatsky Rise (Humphreys et al., 2015; Liu & Currie, 2016; Liu & Gurnis, 2010; Livaccari et al., 1981; Saleeby, 2003). Despite differences in details, several geodynamic models have indicated that the conjugate Shatsky Rise, if it existed, would have collided with North America near what is now southern California between 90 and 85 Ma and generally moved in a northeast arcuate path across the Colorado Plateau, Colorado Rocky Mountains and the Great Plains between 85 and 65 Ma (Figure 1a; Liu & Gurnis, 2010; Humphreys et al., 2015). During the late Campanian to Paleogene (starting at ca. 75 Ma), deformation within the CFB became dominantly thick-skinned (i.e., Laramide orogeny), and the CFB became locally segmented by intraforeland Laramide-style basement-cored uplifts (Bartschi et al., 2018; Dickinson et al., 1988; Lawton, 2008; Lynds & Xie, 2019; Yonkee & Weil, 2015) (Figure 1). These Laramide-style uplifts can cause flexure in adjacent areas and likely would locally interfere with the flexural subsidence caused by loading of the Sevier fold-thrust belt and mantle-induced dynamic subsidence (Aschoff & Steel, 2011; Heller & Liu, 2016; Li & Aschoff, 2022a; Saylor et al., 2020).

The combined effects of flexural loading, dynamic subsidence and global eustatic high throughout the Late Cretaceous resulted in the development of an epicontinental seaway known as the Western Interior Seaway (WIS; Kauffman, 1977; Kauffman, 1985; Chang & Liu, 2020). The most extensive flooding of the seaway occurred in the early Turonian when the WIS extended from the Arctic Ocean to the Gulf of Mexico, and more than one-third of North America was inundated (Figure 1). Deposition during the early Late Cretaceous was characterized by fully marine to marginal marine systems fed by nonmarine systems derived from the Sevier fold-thrust belt to the west (Laskowski et al., 2013). After the peak transgression during the early Turonian, the WIS gradually retreated from the continental interior but was interrupted by several second-order eustatic transgressive-regressive cycles (Kauffman, 1977). The withdrawal of the WIS led to the east- to northeast-directed progradation of shorelines and more widespread nonmarine alluvial-plain to coastal-plain sedimentation in the foreland basin as nonmarine depositional systems fed these prograding shorelines (Bartschi et al., 2018; Li & Aschoff, 2022b). Throughout the Late Cretaceous, the estimated water depth within the WIS never exceeded more than a few hundred meters deep (Kauffman, 1985; Sageman & Arthur, 1994; Weimer, 1984).

3 | METHODS AND DATASET

This study focuses on the Upper Cretaceous strata in Wyoming, Utah, Colorado and New Mexico (Figure 1) and is based on the same regional chronostratigraphic framework used to construct isopach maps in Li and Aschoff (2022a). The Upper Cretaceous strata in the study area were divided into four chronostratigraphic intervals based on ammonite biostratigraphy, sequence stratigraphy and geochronologic data, and four isopach maps spanning 100.5–90.2 Ma, 90.2–80.2 Ma, 80.2–74.6 Ma and 74.6–66 Ma were produced using a total of 627 geophysical well logs (260 of which contain the entire Late Cretaceous interval; Li & Aschoff, 2022a). The general workflow of extracting tectonic subsidence through 3D flexural backstripping is summarized in the following three steps. For each chronostratigraphic interval: (1) a decompacted sediment thickness (i.e., total subsidence) map with a grid resolution of 5 km by 5 km was developed based on decompaction results of selected well logs, (2) the spatial distribution of flexure due to sediment loading was calculated from the decompacted sediment thickness map using gFlex (Wickert, 2016), an open-source Python script that solves the general flexure equation and (3) the tectonic subsidence was derived by subtracting the

calculated flexure from the total subsidence (Watts, 2001). The detailed procedures, as well as uncertainties and errors, involved in each step are described below.

3.1 | Decompaction and development of total subsidence maps

Decompaction corrects the effects of sediment compaction and restores the stratal thickness to the original depositional thickness in the absence of overburden. The decompacted sediment thickness, incorporated with changes in paleowater depth, represents the total subsidence (Allen & Allen, 2013; Angevine et al., 1990; Steckler & Watts, 1978). With a porosity-depth relationship and the assumption that the rock grain volume is conserved during compaction, decompaction is a fairly straightforward process. This study followed the standard procedure of decompaction described in Angevine et al. (1990) and Allen and Allen (2013). The empirical porosity-depth relationships and compaction constants used for different lithologies are from Sclater and Christie (1980).

Although this study focuses on only the Upper Cretaceous strata, compaction was not limited to just these strata; rather, it occurred over the entire sedimentary cover above the crystalline basement. Ignoring the compaction of overlying and underlying strata would lead to inaccurate decompacted sediment thickness of the Upper Cretaceous strata (Pang, 1995). Therefore, 223 relatively deep wells (i.e., wells containing Upper Cretaceous and post-Cretaceous strata) for decompaction were selected because the thickness of post-Cretaceous strata can be better constrained. The remaining 404 well logs used in the dataset either contain incomplete Upper Cretaceous strata or are located near uplifted areas. The thickness of pre-Upper Cretaceous strata was determined based on the difference between the basement depth (Marshak et al., 2017) and the depth at the base of the Upper Cretaceous strata. The stratigraphic framework (average lithology vs. age) used in decompaction differs across the study area for the Upper Cretaceous strata and is summarized in Appendix A in Supporting Information. For both the pre- and post-Upper-Cretaceous strata, an average shaly sandstone lithology was used. The decompaction results were also divided into the same four chronostratigraphic intervals spanning 100.5–90.2 Ma, 90.2–80.2 Ma, 80.2–74.6 Ma and 74.6–66 Ma. The API of all decompacted well logs and decompaction results are provided in the Supporting Information.

For the 223 well logs that were decompacted based on empirical porosity-depth relationships, strong linear relationships ($R^2 > .92$) exist between the stratal thickness and decompacted sediment thickness for all four

chronostratigraphic intervals (Figure 2). The linear regression equations between stratal thickness and total subsidence (Figure 2) were then applied to the remaining 404 well logs that contain only partial Upper Cretaceous strata (due to uplift or shallow well depth) to calculate the decompacted sediment thickness from the stratal thickness of a given chronostratigraphic interval. This step provides more control points to better constrain the spatial variability in decompacted sediment thickness by incorporating more well logs that cannot be appropriately decompacted. For each chronostratigraphic interval, the amount of decompacted sediment thickness at areas away from the control points was interpolated in ArcGIS using a natural neighbour technique to develop a decompacted sediment thickness map with a grid resolution of 5 km (both horizontal and vertical). The natural neighbour technique was selected over other interpolation methods (e.g., inverse distance weighing and kriging) because: (1) the interpolated results best represent the data and are virtually free of interpolation artefacts and (2) the transitions between data points are smooth.

Theoretically, once compaction corrections have been made, the change in water depth (ΔW_d) during a given chronostratigraphic interval is simply added in to produce the total subsidence. However, for the purpose of this study, changes in water depth can be considered negligible. This is particularly the case for the 90.2–80.2 Ma and 80.2–74.6 Ma chronostratigraphic intervals because the paleoshoreline shoreline and the distribution of different paleogeographic environments (intimately linked to water depth) did not change significantly during these two time intervals (Li & Aschoff, 2022b)—most part along the generally north–south-oriented paleoshoreline shifted <100 km laterally (westward or eastward) during each time interval (Figure 3). For the 100.5–90.2 Ma and 74.6–66 Ma time intervals, the areas with the largest decompacted sediment thickness correspond to continental to proximal shallow marine environments (<100 km from the paleoshoreline; Li & Aschoff, 2022b)—changes in water depth at these areas are much smaller in magnitude (<5%) compared to the largest decompacted sediment thickness.

Admittedly, neglecting changes in water depth would underestimate and overestimate the total subsidence in the distal (eastern) areas (where water depth was supposedly the largest) for the 100.5–90.2 Ma and 74.6–66 Ma time intervals, respectively. This is because the eastern study area experienced
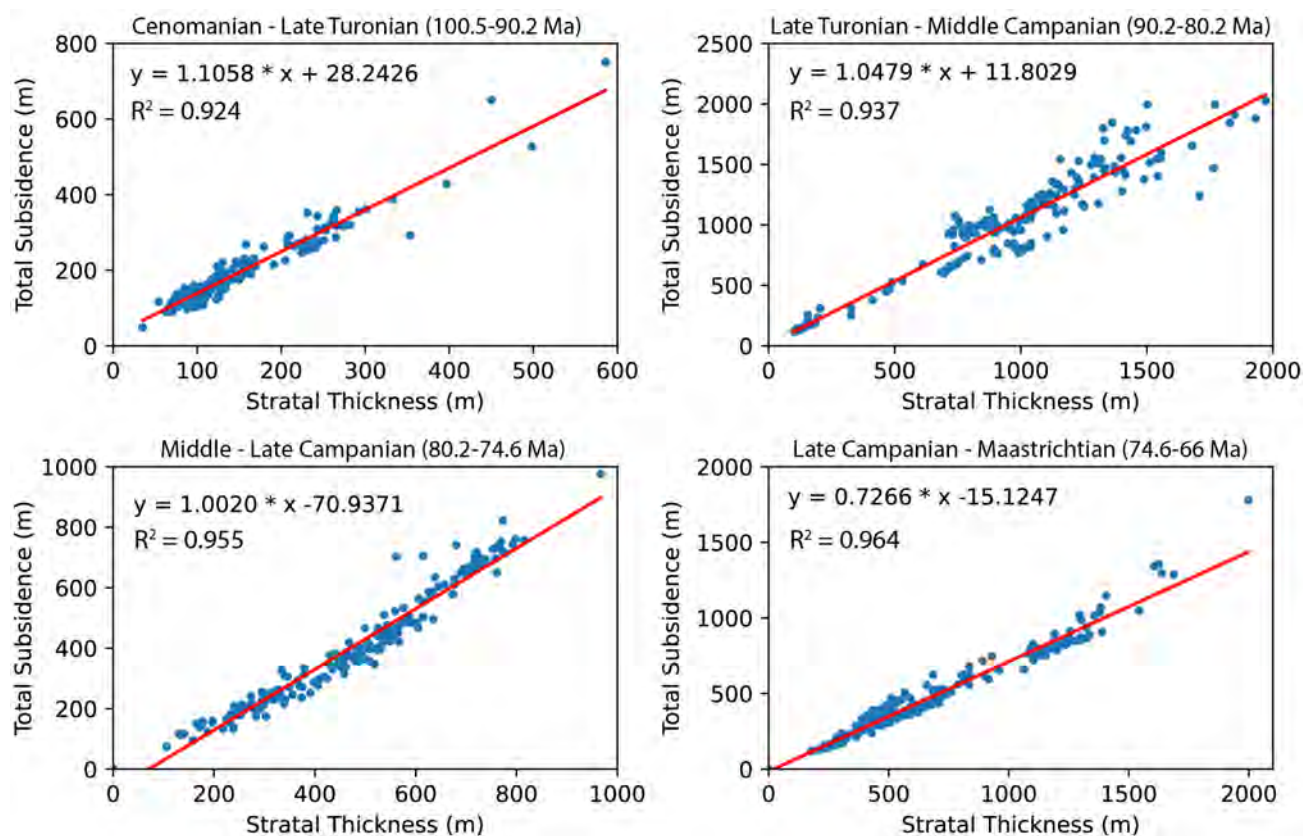

FIGURE 2 Strong linear relationships exist between the stratal thickness and total subsidence for all four chronostratigraphic intervals focused in this study. Data points for each plot are the same and from the 223 wells used for decompaction (indicated by red dots in Figure 1b).
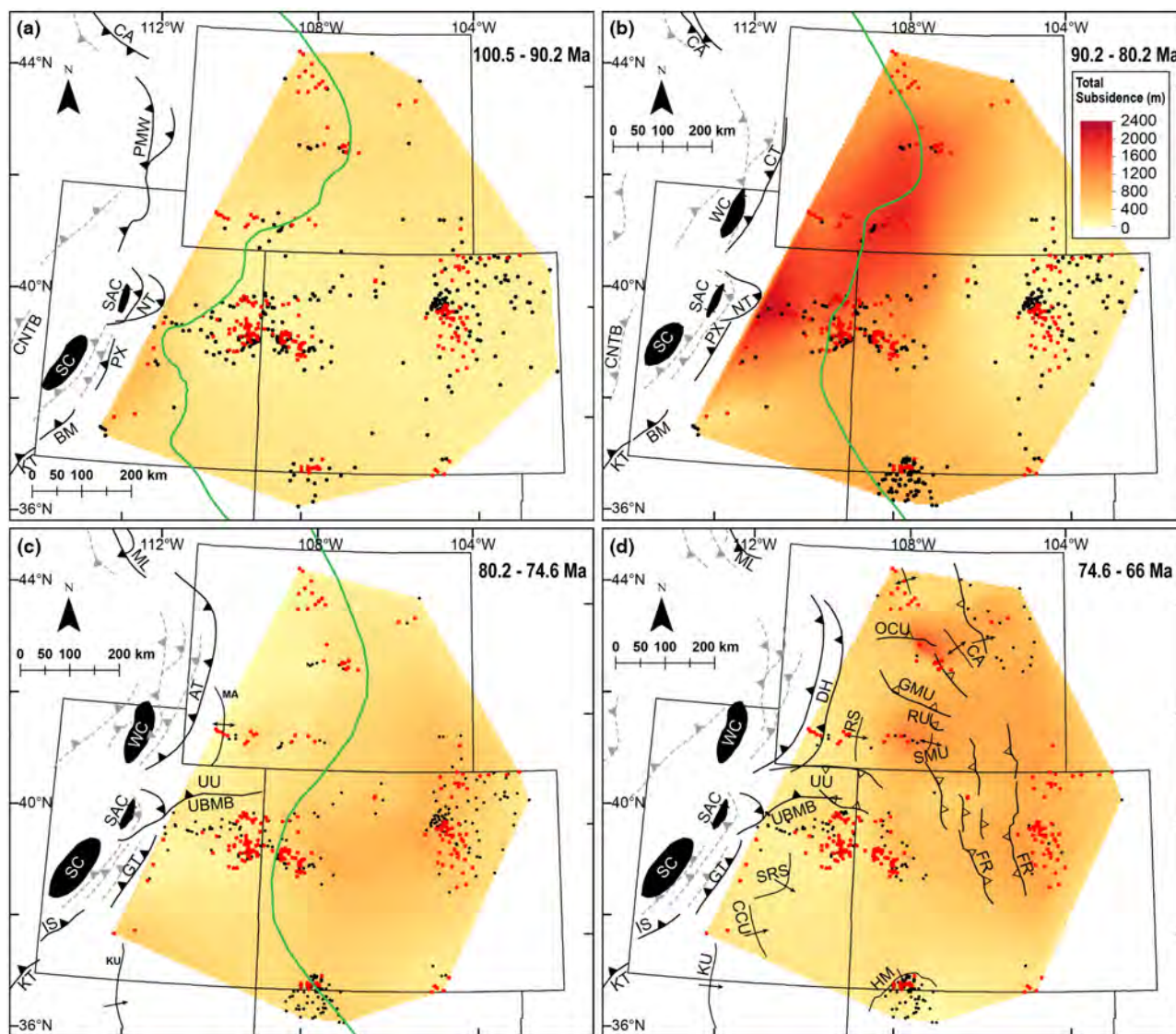
FIGURE 3 Decompacted sediment thickness (i.e., total subsidence) maps of Cenomanian to late Turonian (100.5–90.2 Ma; a), late Turonian to middle Campanian (90.2–80.2 Ma; b), middle Campanian to late Campanian (80.2–74.6 Ma; c), middle Campanian to Maastrichtian (74.6–66 Ma; d). For each map, red dots indicate well logs used for decompaction, whilst the decompacted sediment thickness at well logs marked by black dots was calculated using the empirical relation shown in Figure 2. The total subsidence pattern resembles the isopach pattern (Li & Aschoff, 2022a) due to the strong linear relationships between stratal thickness and decompacted sediment thickness (Figure 2). The shoreline locations at 90.2, 80.2 and 74.6 Ma are shown in (a), (b) and (c), respectively. The study area was dominated by continental environments at 100.5 and 66 Ma. The legend and abbreviations for structural features can be found in Figure 1.

overall transgression and regression during the 100.5–90.2 Ma and 74.6–66 Ma, respectively. Still, the magnitude of water depth change in the eastern study area during these two time intervals is likely <100 m (Heller & Liu, 2016; Pang, 1995), <10% of the largest decompacted sediment thickness (i.e., ca. 800 m for 100.5–90.2 Ma and 1800 m for 74.6–66 Ma). Based on the above reasons, the decompacted sediment thickness maps were considered good representations of total subsidence maps for the four time intervals. Another practical reason not to correct water depth on the map scale is the rather limited number

of unequivocal control points of water depth across the study area, which may lead to significant and unexpected errors when interpolating the water-depth change between control points. Without a confident map illustrating the change in water depth across the study area during each chronostratigraphic interval, it is meaningless to correct the corresponding decompacted sediment thickness maps. Therefore, the decompacted sediment thickness maps were used as substitutes for total subsidence maps, which served as input data to calculate the flexure due to sediment loading in the next step.

TABLE 1 Parameters used to calculate flexure due to sediment loading in gFlex. The corresponding elastic thickness of 10^{23}, 10^{24} and 4×10^{24} Nm are 22.4, 48.3 and 76.6 km, respectively

Parameter	Value
Young's modulus (GPa)	100
Poisson's ratio	0.25
Mantle density (kg/m^3)	3300
Sediment density (kg/m^3)	2300
Lithospheric rigidity (Nm)	10^{23}, 10^{24}, 4×10^{24} and uniform increase from west (10^{23}) to east (4×10^{24})
Gravitational acceleration (m/s^2)	9.81
Computation interval (m)	5000
North, south, west, east boundary condition	Mirror

3.2 | Flexural unloading of sediment

The original input grid (total subsidence map) was first expanded (by extrapolating the last values from the edge) to about 15% from all sides to become a rectangular grid to avoid edge effects following a similar 3D flexural backstripping procedure described in Colleoni et al. (2021). Next, the flexure due to sediment loading was calculated from each expanded total subsidence map using gFlex (Wickert, 2016), a software package designed to compute flexural deflection for Earth's surface. The expression of two-dimensional flexure based on the general analytical solution is (Turcotte & Schubert, 2002):

$$D\nabla^4\omega(x) = D\frac{\partial^4\omega}{\partial x^4} + D\frac{\partial^4\omega}{\partial y^4} + 2 - D\frac{\partial^4\omega}{\partial x^2\partial y^2} + \Delta\rho g\omega = q$$

where ω is the vertical deflection of the plate (m), $\Delta\rho$ is the density contrast (kg/m^3) between the mantle and the loading material (water, sediment or a combination of the two), g is the gravitational acceleration (m/s^2) and q (Pa) is the thrust load function in foreland basin modelling and the sediment load function in flexural backstripping. D is the flexural rigidity (Nm) of an elastic plate defined as:

$$D = \frac{ET_e^3}{12(1-v^2)}$$

where E is Young's modulus (Pa), v is Poisson's ratio (dimensionless) and T_e is the effective elastic thickness (m) of the plate.

A Young's modulus of 100 GPa was used in this study for consistency with the estimations of T_e of the North American lithosphere (Bechtel et al., 1990), and the choice of Poisson's ratio equal to 0.25 is consistent with other similar studies (Jordan, 1981; Tufano & Pietras, 2017; White et al., 2002). Flexural rigidity is an extremely important parameter in any flexural modelling, but unfortunately, it

is difficult to constrain because: (1) T_e of the continents has a wide range of values (from 5 to over 100 km; Tesauro et al., 2015) and (2) it remains poorly known what portion of the lithosphere behaves elastically on a geological time scale (Angevine et al., 1990). Therefore, four conditions of flexural rigidities (equivalent elastic thickness and sources in parentheses) consistent with those used in previous studies of foreland basins were used in this study to examine the effects of flexural rigidity on the flexural backstripping results. Under the first three conditions, the lithospheric rigidity was assumed to be constant across the study area as 10^{23} Nm (22 km; Jordan, 1981; Liu et al., 2014), 10^{24} Nm (48 km; Heller et al., 1988; Pang & Nummedal, 1995), 4×10^{24} Nm (77 km; Painter & Carrapa, 2013). Under the fourth condition, the lithospheric rigidity was assumed to uniformly increase eastward from 10^{23} to 4×10^{24} Nm across the study area, consistent with the eastward increase in effective elastic thickness suggested by Bechtel et al. (1990); Saylor et al. (2020). The effective elastic thickness across the study area was also likely subject to temporal changes (Saylor et al., 2020), highlighting the need of considering different lithospheric rigidity conditions. A constant sediment density (2300 kg/m^3) was used to calculate flexure caused by loading caused by infilling (partially compacted) sediments. Input parameters used to calculate the flexure due to sediment loading in gFlex are summarized in Table 1.

The remaining subsidence was calculated by subtracting the sediment-induced flexure calculated using gFlex from the total subsidence calculated in step 1 (Watts, 2001). The subtraction was performed only in the original input grid (total subsidence map without expansion). It is important to note that the remaining subsidence still is a composite of tectonics subsidence (regardless of origin), eustatic sea-level change and related effects of water loading and water depth. The effect of ecstatic sea-level change can be neglected based on two reasons. First, the Late Cretaceous is generally

considered a period of long-term eustatic high characterized by small changes in sea level. According to the eustatic history reconstructed from eastern North America's passive margin, the magnitude of eustatic changes during each of the four selected time intervals is <25 m (Miller et al., 2005; Kominz et al., 2008). Such a small range in sea-level change would only result in <36 m subsidence based on local (Airy) isostasy. Second, an unequivocal reconstruction of the Late Cretaceous eustasy is still lacking. Although many previous studies have attempted to reconstruct the past eustatic history at supposedly tectonically stable passive margins, the lithospheric vertical motions in these areas have been increasingly documented as subject to dynamic topography, the effects of which have not been removed (Morris et al., 2020; Moucha et al., 2008). Therefore, it is probably safer to ignore the effects of eustatic changes for the purpose of this study at this stage. The effects of water depth and water loading can also be considered negligible (subtracting water loading from water depth would even lessen the effects of water depth) based on the reasons outlined in Section 3.1. The remaining subsidence was therefore attributed mainly to tectonic subsidence.

4 | OBSERVATIONS: SPATIO-TEMPORAL PATTERNS IN TECTONIC SUBSIDENCE

For each of the four chronostratigraphic intervals, one total subsidence map (Figure 3) and four tectonic subsidence maps (Figures 4–7) were developed. Although the first-order trend revealed by the tectonic subsidence map is generally consistent with the total subsidence map (or isopach map) for each time interval, the tectonic subsidence map provides better constraints on the magnitude and areal extent of tectonic subsidence and uplift. The subsidence (and uplift) pattern is generally consistent in the tectonic subsidence maps developed under different lithospheric rigidity conditions for all four chronostratigraphic intervals, with the maximum subsidence/uplift distinctly changing in areal extent and magnitude depending on the rigidity used—the extent and magnitude of the maximum subsidence/uplift become larger when a higher rigidity was used (Figures 4–7).

Cenomanian to late Turonian (100.5–90.2 Ma) tectonic subsidence maps reveal the maximum tectonic subsidence (ca. 400 m) located in central Utah (Figure 4). Tectonic subsidence rapidly decreases in magnitude from central Utah eastward, and the minimum tectonic subsidence (the smallest positive tectonic subsidence) or even up to ca. 60 m tectonic uplift (negative tectonic subsidence) depending on the rigidity scenario was located in northeastern Utah

(Figure 4). This area of minimum tectonic subsidence or uplift expands further eastward by ca. 100 km (to northwestern Colorado) when a higher lithospheric rigidity is used (Figure 4c). Other than the Moxa Arch area, which shows up to 30 m of uplift, the Wyoming part of the study area shows overall low to moderate (<200 m) tectonic subsidence for this time interval (Figure 4), and most of Colorado is characterized by <100 m tectonic subsidence.

Late Turonian to middle Campanian (90.2–80.2 Ma) tectonic subsidence maps indicate maximum tectonic subsidence (ca. 1200 m) located in north-central Utah, from where tectonic subsidence generally decreases in magnitude eastward (Figure 5). An area of moderately large tectonic subsidence (up to ca. 800 m) is located in southwestern Wyoming. The area of maximum tectonic subsidence in north-central Utah and the area of moderate tectonic subsidence are separated by an area of relatively low tectonic subsidence (<400 m) in the southwestern corner of Wyoming (the Moxa Arch area). Tectonic subsidence rapidly decreases in magnitude from southwestern Wyoming eastward (Figure 5). Another area with moderate tectonic subsidence (ca. 400 m) during this time is the Four Corners area (especially northwestern New Mexico). Two distinct areas of uplift (or very low tectonic subsidence) are located in southern Utah and northern Colorado (to southeastern Wyoming). These two areas of uplift (or very low tectonic subsidence) also expand in extent when a higher lithospheric rigidity was used (Figure 5).

Middle to late Campanian tectonic (80.2–74.6 Ma) subsidence maps show a distinctly different tectonic subsidence pattern compared to the earlier two chronostratigraphic intervals. The main area of tectonic subsidence (300–400 m) is located in central Colorado to southeastern Wyoming (Figure 6). Three other areas of moderate tectonic subsidence (200–300 m) seem to be located in the east of the Moxa arch, southern Utah (the Kaiparowits Plateau region) and northwestern New Mexico. A local area of small tectonic subsidence (100–200 m) seems to occur south of the Uinta uplift (Figure 6). All other areas, especially areas in front of the Sevier fold-thrust belt, are characterized by very low tectonic subsidence (<100 m) or even uplift (up to ca. 150 m; Figure 6).

Middle Campanian to Maastrichtian (74.6–66 Ma) tectonic subsidence maps show a broad, composite area of tectonic subsidence extending from north-central Colorado to eastern Wyoming. This composite area comprises at least four subareas of large tectonic subsidence (>400 m), including Wind River Basin (up to 1400 m), Washakie Basin (600–800 m), Powder River Basin (400–600 m) and western Denver Basin (400–600 m), separated by areas of uplifts or low tectonic subsidence (<200 m). Most areas other than the broad area of tectonic subsidence show overall low tectonic subsidence (<200 m) or uplift.
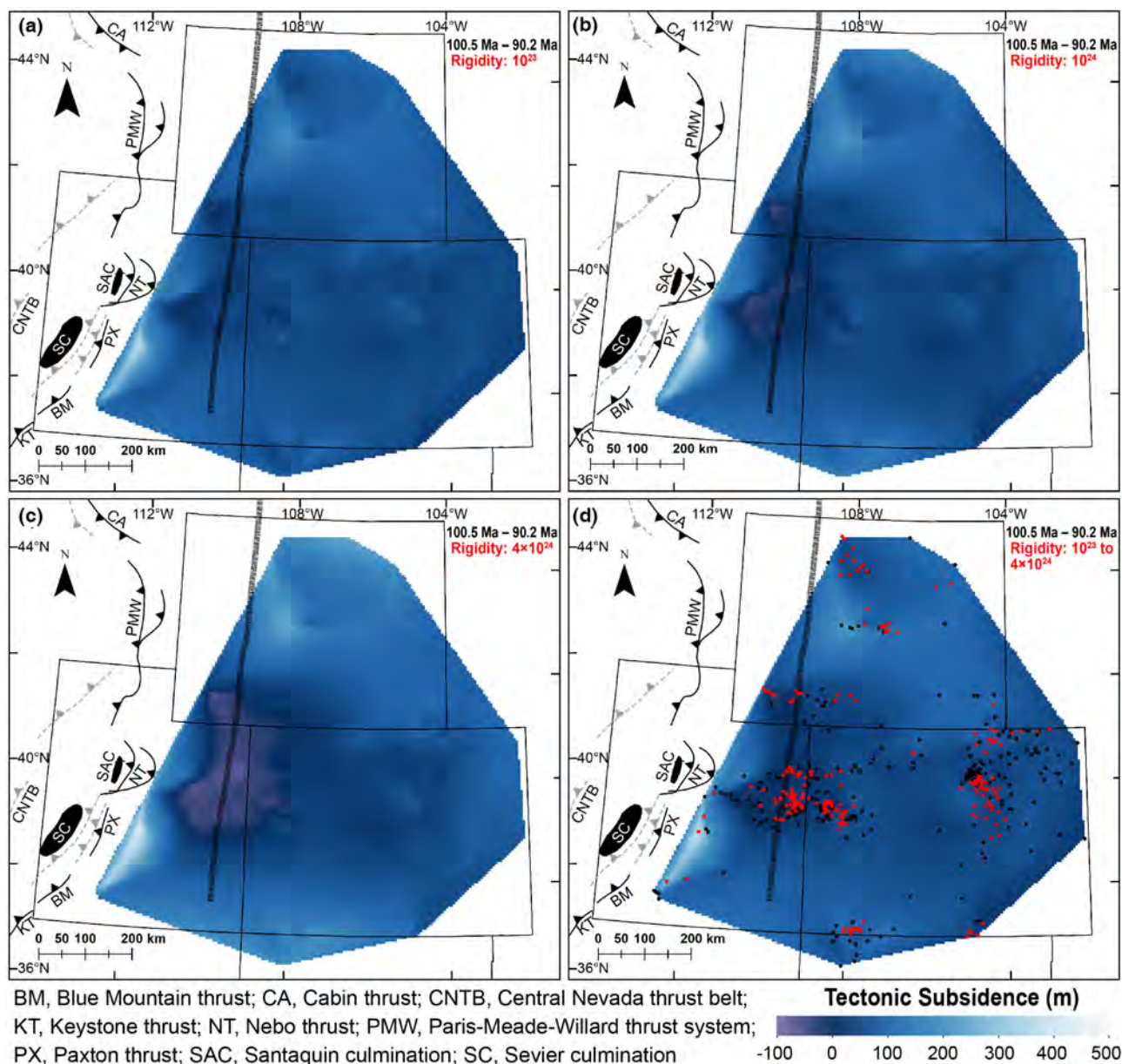
FIGURE 4 Cenomanian to late Turonian (100.5–90.2 Ma) tectonic subsidence maps developed using different rigidity conditions show the maximum tectonic subsidence (ca. 400 m) is located in central Utah. The lithospheric rigidity is constant in a (10^{23} Nm), b (10^{24} Nm) and c (4×10^{24} Nm) across the study area and uniformly increases from west (10^{23} Nm) to east (4×10^{24} Nm) in (d). Note the areal extent and magnitude of tectonic uplift at northeastern Utah become larger when a larger rigidity was used (a–c). The active versus inactive Sevier thrusts and approximate location of forebulge (thick shaded line) during Turonian are from DeCelles (2004). Well log control points used to develop all four maps are the same and are only indicated in (d). Red dots indicate well logs used for decompaction. See Figure 1 for legend of structural features. The colour ramp used in all tectonic subsidence maps (Figures 4–7) is consistent.

5 | INTERPRETATION: DISCRIMINATION OF DIFFERENT TECTONIC SUBSIDENCE MECHANISMS

As the first regional application of 3D flexural backstripping in the CFB, the new tectonic subsidence maps presented herein provide more accurate insights into the complex tectonic history of the Late Cretaceous CFB compared to stratal thickness pattern revealed by earlier isopach maps or flexurally backstripped 2D cross-sections, within which the flexure due to sediment loading has not been fully removed. In this section, the temporal and spatial variations in the effects of different tectonic subsidence mechanisms are first discussed based on the new tectonic subsidence maps described above and three tectonic subsidence profiles (Figure 8) across the central part of the study area (better constrained by control points). The new and more quantitative constraints of the
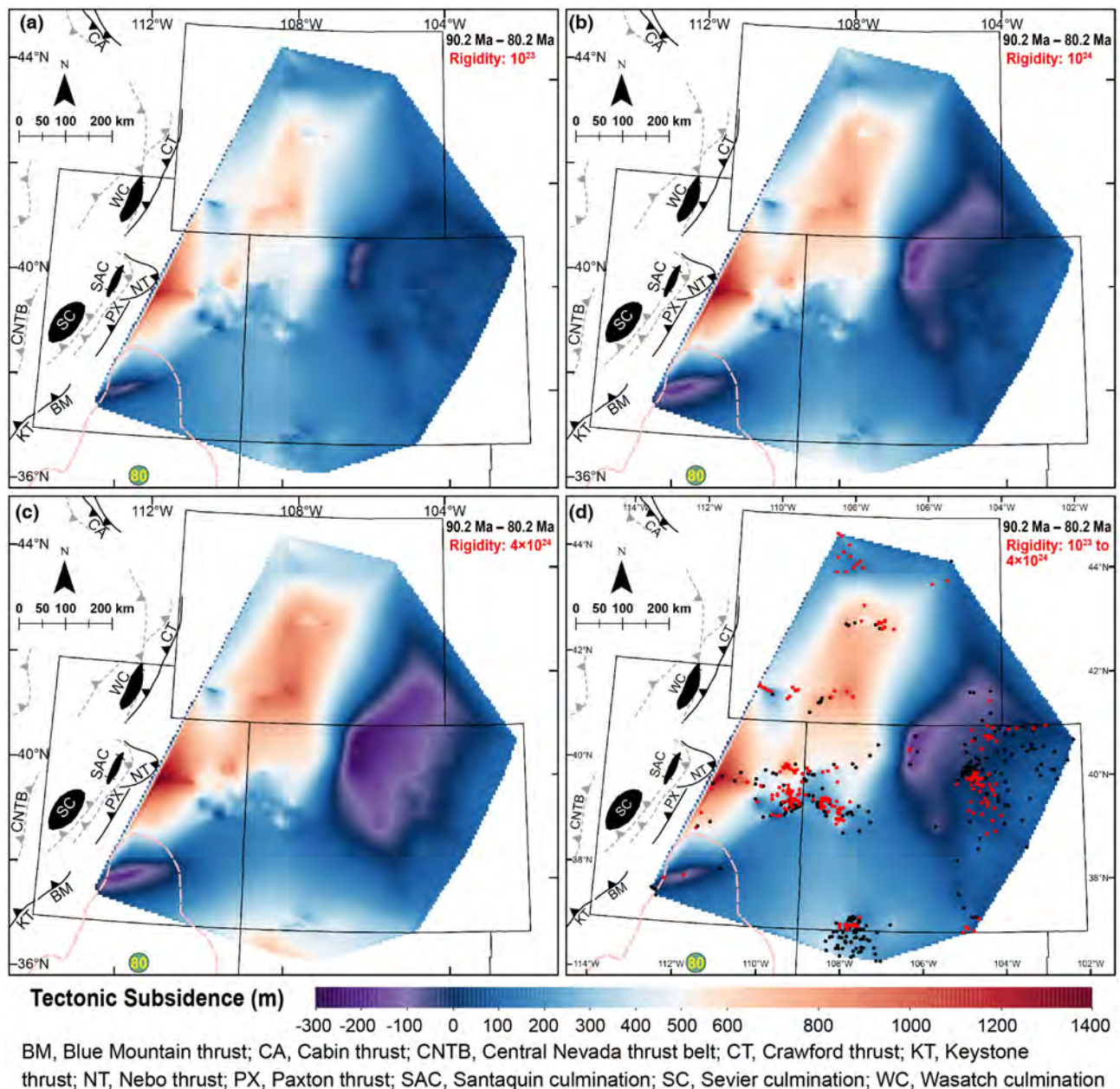
Tectonic Subsidence (m)

-300 -200 -100 0 100 200 300 400 500 600   800   1000   1200   1400

BM, Blue Mountain thrust; CA, Cabin thrust; CNTB, Central Nevada thrust belt; CT, Crawford thrust; KT, Keystone thrust; NT, Nebo thrust; PX, Paxton thrust; SAC, Santaquin culmination; SC, Sevier culmination; WC, Wasatch culmination

FIGURE 5 Late Turonian to middle Campanian (90.2–80.2 Ma) tectonic subsidence maps developed using different rigidity conditions reveal the maximum tectonic subsidence (ca. 1200 m) is located in north-Central Utah. The lithospheric rigidity is constant in a (10^{23} Nm), b (10^{24} Nm) and c (4×10^{24} Nm) across the study area and uniformly increases from west (10^{23} Nm) to east (4×10^{24} Nm) in (d). The shape of the conjugate Shatsky Rise at ca. 80 ma (from Humphreys et al., 2015) is outlined by red dashed lines. Coniacian to Santonian active versus inactive Sevier thrusts are from DeCelles (2004). Well log control points used to develop all four maps are the same and are only indicated in (d). Red dots indicate well logs used for decompaction. See Figure 1 for legend of structural features.

effects of dynamic topography revealed in this study are discussed in the next section (Section 6).

5.1 | Cenomanian to late Turonian (100.5–90.2 ma)

During the Cenomanian to late Turonian, the tectonic subsidence pattern in the southern part of the study area

(Utah to Colorado; cross-sections BB' and CC' in Figure 8) well conforms to the flexural subsidence profile generated by a topographic loading (DeCelles & Giles, 1996), reflecting dominant flexural subsidence in response to loading of the Sevier fold-thrust belt. Central Utah (in front of the Paxton thrust) was located at the foredeep. A distinct forebulge was located in northeastern Utah (to northwestern Colorado when a larger lithospheric rigidity was used; Figure 4). Most of Colorado was in the backbulge region
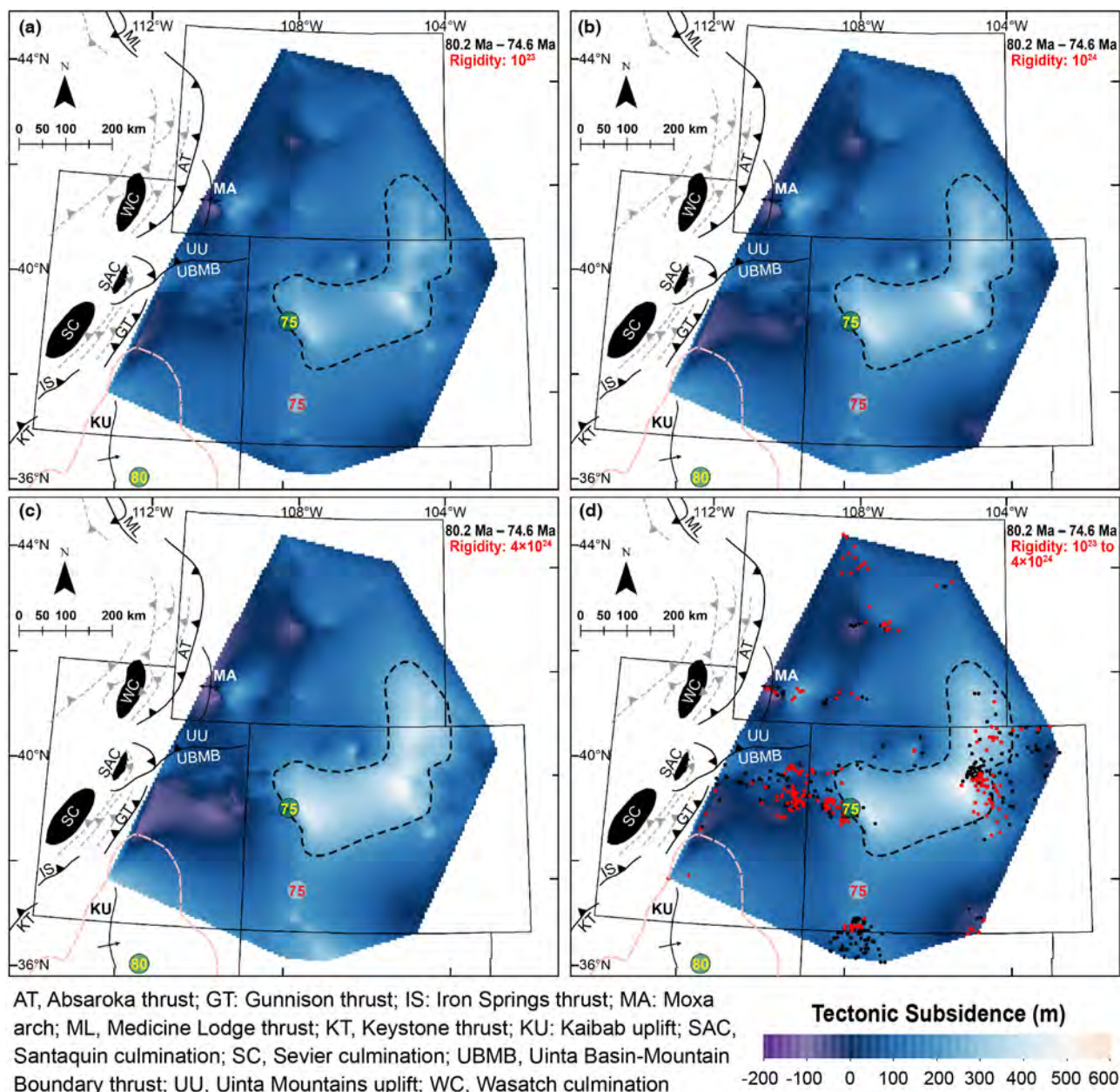
FIGURE 6 Middle to late Campanian (80.2–74.6 Ma) tectonic subsidence maps developed using different rigidity conditions show the main area of tectonic subsidence (300–400 m) is located from central Colorado to southeastern Wyoming. The lithospheric rigidity is constant in a (10^{23} Nm), b (10^{24} Nm), and c (4×10^{24} Nm) across the study area and uniformly increases from west (10^{23} Nm) to east (4×10^{24} Nm) in (d). The broad area of tectonic subsidence from north-central Colorado to southeastern Wyoming can be mostly attributed to dynamic subsidence. Regardless of the lithospheric rigidity, an irregular-shaped (i.e., lunate) subregion (ca. 450 by 150 km) of dynamic subsidence (>200 m) persists (dashed outlines). The shape of the conjugate Shatsky Rise at ca. 80 Ma (from Humphreys et al., 2015) is outlined by red dashed lines. Campanian active versus inactive Sevier thrusts are from DeCelles (2004). Active Laramide-style uplifts (Kaibab uplift and moxa arch) during this time interval are from Li and Aschoff (2022b). Well log control points used to develop all four maps are the same and are only indicated in (d). Red dots indicate well logs used for decompaction. See Figure 1 for legend of structural features.

(Figures 4 and 8). Meanwhile, a distinct foredeep is not present in the Wyoming part of the study area, probably due to the limited extent of the study area (Figure 4). The Moxa Arch area, characterized by minor uplift, is likely the forebulge (Figure 8). In this sense, areas east of the

Moxa Arch in Wyoming were interpreted as located in the backbulge region (Figure 4).

It is interesting to note that the forebulge location revealed by tectonic subsidence maps developed through 3D flexural backstripping, especially if the lithosphere is
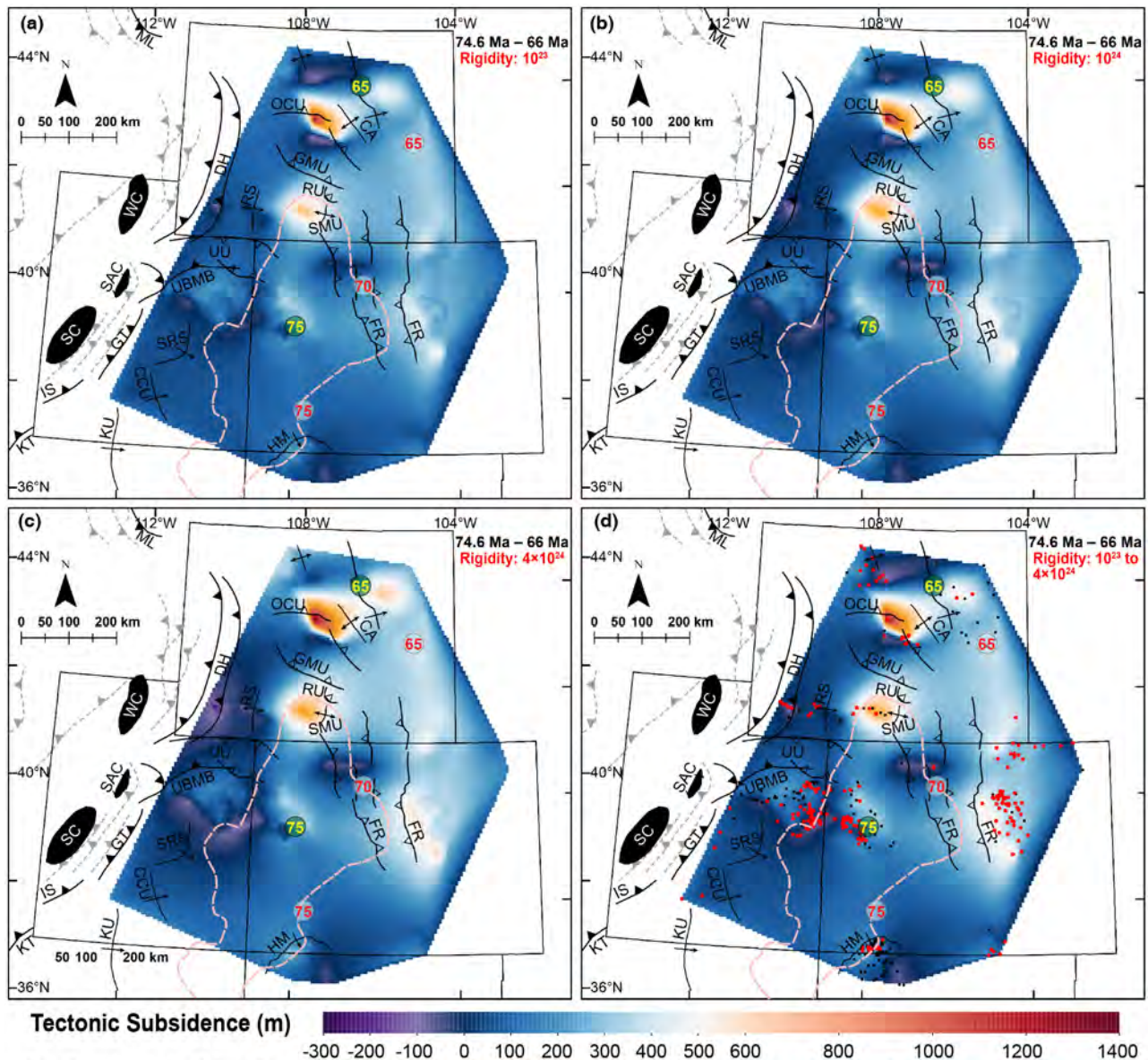
FIGURE 7 Late Campanian to Maastrichtian (74.6–66 Ma) tectonic subsidence maps developed using different rigidity conditions show a broad, composite area of tectonic subsidence extending from north-central Colorado to eastern Wyoming. The study area was segregated by common Laramide-style uplifts during this time, which may lead to interpolation artefacts—The pattern in areas far away from control points should be viewed with caution. The lithospheric rigidity is constant in a (10^{23} Nm), b (10^{24} Nm) and c (4×10^{24} Nm) across the study area and uniformly increases from west (10^{23} Nm) to east (4×10^{24} Nm) in (d). Tectonic subsidence from north-central Colorado to eastern Wyoming is interpreted to be the combined result of flexural subsidence due to lithospheric loading of adjacent Laramide-style uplifts (local sub-depocenters) and a component of dynamic subsidence in front of the modelled position of the conjugate Shatsky Rise. The shape of the conjugate Shatsky Rise at ca. 75 Ma (from Humphreys et al., 2015) is outlined by red dashed lines. Maastrichtian active versus inactive Sevier thrusts are from DeCelles (2004). Active Laramide-style uplifts during this time interval are from Li and Aschoff (2022b). Well log control points used to develop all four maps are the same and are only indicated in (d). Red dots indicate well logs used for decompaction. See Figure 1 for legend of structural features.

relatively less rigid, is slightly west (closer to the thrust front) of that indicated by isopach maps (Figure 4; DeCelles, 2004). This highlights the flexural effects of

sediment loading and extra caution needed when using stratal thickness profile as a proxy for foreland basin profile—sediments filling the foredeep would generate
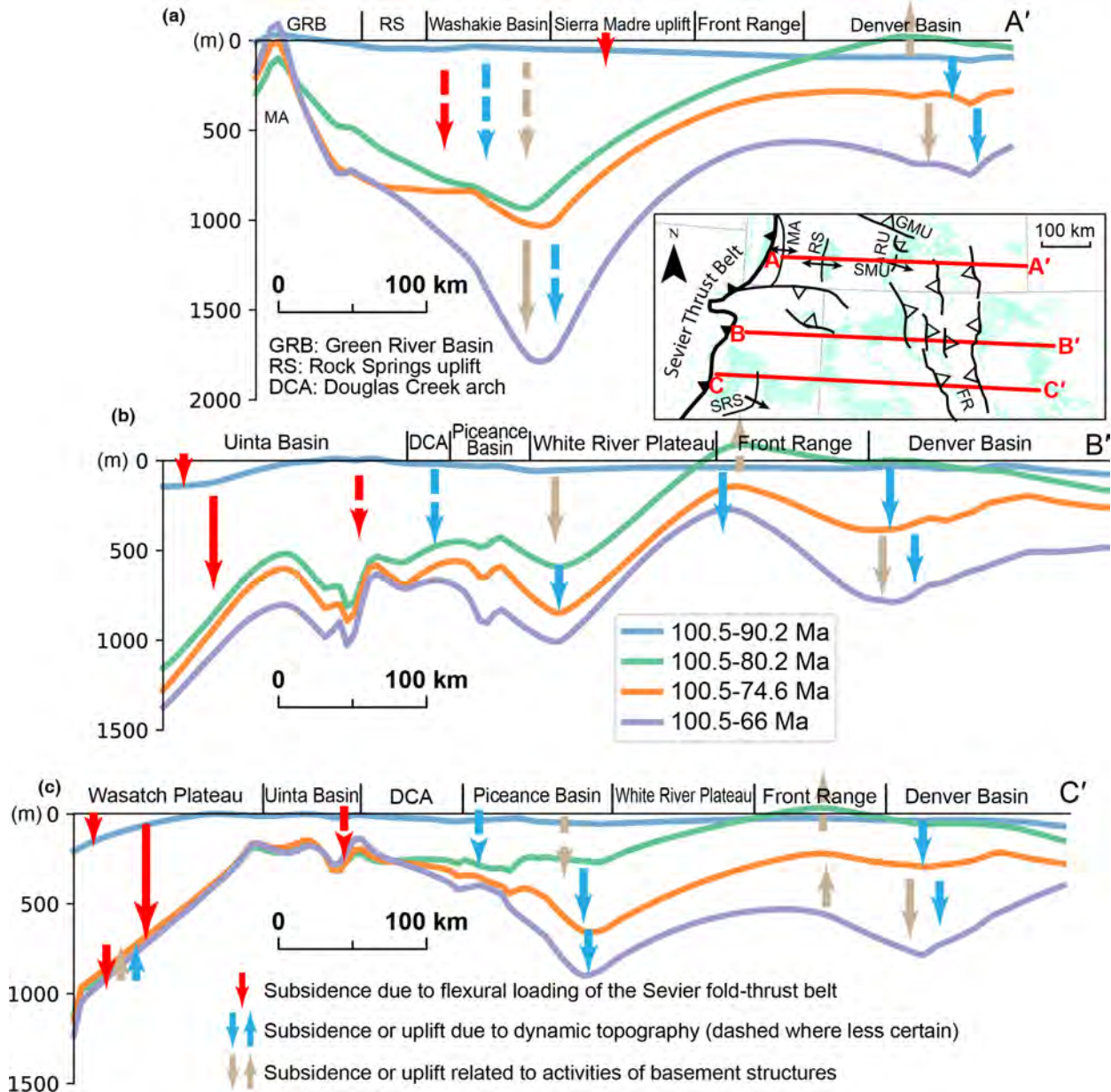
FIGURE 8 Tectonic subsidence profiles across AA', BB' and CC' based on 3D flexural backstripping results under the fourth condition of flexural rigidity (i.e., lithospheric rigidity uniformly increases eastward from 10^{23} to 4×10^{24} Nm across the study area). The regional tectonic subsidence pattern for a given time interval is generally consistent regardless of the flexural rigidity condition. Each tectonic subsidence profile represents the cumulative tectonic subsidence since the Cenomanian (100.5 Ma).

flexure to 'displace' the forebulge away from the thrust front. With the flexure generated by sediment loading appropriately removed through 3D flexural backstripping, the more accurate flexural subsidence pattern in front of the Sevier thrust belt revealed in the new tectonic subsidence maps (e.g., Figures 4 and 5) can provide useful insights into the spatial restoration of the Sevier fold-thrust belt (i.e., load scale and its lateral variability) during different time intervals. No long-wavelength subsidence that can be attributed to mantle-induced dynamic subsidence is present in Figure 4, indicating mantle-induced dynamic subsidence was likely

negligible in the study area during the Cenomanian to late Turonian.

5.2 | Late Turonian to middle Campanian (90.2–80.2 ma)

The main area of tectonic subsidence remained in the western part of the study area during the late Turonian to middle Campanian (Figure 5), indicating that flexural subsidence in response to loading of the Sevier fold-thrust belt continued to be the dominant subsidence mechanism.

A distinct foredeep was located in north-central Utah, directly in front of the Nebo thrust, and a forebulge seems to be located in northeastern Utah (Figure 5). The foredeep in front of the Crawford thrust is, again, probably not captured by the extent of our study area. The Moxa Arch area, characterized by relatively lower tectonic subsidence compared to its surrounding areas, can be linked to the forebulge (Figure 5), which is also consistent with the results of three-dimensional flexural numerical modelling (Luo & Nummedal, 2012). In this sense, areas east of the Moxa Arch in Wyoming would be located in the backbulge zone.

The moderate tectonic subsidence (ca. 400 m) at the Four Corners region most likely represents the long-wavelength dynamic subsidence because it is located >400 km from the nearest thrust front in southwestern Utah (Figure 5). Considering the modelled location of the conjugate Shatsky Rise at ca. 85 Ma (Figure 1), the dynamic subsidence at the Four Corners region can be attributed to mantle downwelling flows in front of the buoyant oceanic plateau. Some additional patterns during this time interval may also hint at the influence of dynamic subsidence in the study area. Particularly, the tectonic subsidence pattern in the supposedly forebulge and backbulge regions during 90.2–80.2 Ma (Figure 8) does not conform to an idealized flexural profile—uplift or negligible at the forebulge and minor (a few tens of meters) subsidences in the backbulge region (DeCelles & Giles, 1996). In both the southern and northern parts of the study area, the forebulge was relatively stationary (i.e., northeastern Utah and the Moxa Arch area) since the Cenomanian (Figure 8). The significant amount of tectonic subsidence, as well as the eastward increases in the magnitude of tectonic subsidence from the forebulge to ca. 200 km east of it (e.g., from the Moxa Arch area to southern Wyoming in AA′ and from the eastern Uinta Basin to the Piceance Basin in cross-sections BB′ and CC′ in Figure 8), cannot be explained by only flexural subsidence generated by a topographic load. Thus, the up to 800 and 500 m tectonic subsidence in southwestern Wyoming and from northeastern Utah to the Piceance Basin, respectively, likely indicates additional subsidence due to dynamic subsidence (Figure 8). In this sense, dynamic subsidence may have also contributed to the rapid tectonic subsidence in the foredeep zone in north-central Utah during the late Turonian to middle Campanian (up to ca. 120 m/m.y.), which had almost tripled from ca. 40 m/m.y. (mostly flexural subsidence) in central Utah during the Cenomanian to late Turonian, although the increased scale of the Sevier fold-thrust belt may have also played a role.

Further evidence indicative of dynamic topography in the study area during this time is the uplift (200 ± 100 m) in southern Utah, which was located in a supposedly foredeep region. The uplift here cannot be linked to the activity (or quiescence) of the Sevier fold-thrust belt because the thrust segments in southern Utah (e.g., Blue Mountain and Iron Springs thrusts) were documented to be active at this time (DeCelles, 2004). Instead, the uplift in southern Utah can be linked to dynamic uplift, consistent with the modelled location of the overall buoyant conjugate Shatsky Rise below this area by 80 Ma (Figure 5).

The tectonic uplift observed in northern Colorado (extending to southeastern Wyoming) is more enigmatic. One possible explanation for the tectonic uplift in this area is the reactivation of basement faults (Weimer, 1984). It is also possible that the broad area of uplift, as well as the uplift in southeastern Wyoming, are artefacts caused by assuming a flexural rigidity that is too high (Figure 5). Nevertheless, the uplift in northern Colorado persists regardless of different flexural rigidities. The uplift in northern Colorado may be linked to a pulse of early (before 80 Ma) uplift of the northern part of the Front Range, considering the coincidence in the location and extent between the depicted uplifted area and the Front Range (Figures 5 and 8). In this sense, the increased tectonic subsidence in southwestern Wyoming may be linked to flexural subsidence caused by the uplift of the Moxa arch and the Front Range. In this sense, the broad area of tectonic subsidence area from central to southwestern Wyoming may also be an artefact because only two subregions of moderately large tectonic subsidence (i.e., southwestern Wyoming and central Wyoming) are constrained by control points (Figure 5d). And the moderate tectonic subsidence in central Wyoming, therefore, may similarly be linked to some early basement-involved uplifts (e.g., the Owl Creek uplift and the Casper arch).

5.3 | Middle to late Campanian (80.2–74.6 ma)

Tectonic subsidence from central Colorado to southeastern Wyoming (area with >100 m tectonic subsidence in Figure 6) during the middle to late Campanian strongly points to the long-wavelength dynamic subsidence based on the large distance (ca. 500 km) away from the Sevier thrust fronts because a topographic load is unlikely to generate any distinct flexural topography at >300 km away (DeCelles & Giles, 1996; Jordan, 1981; Painter & Carrapa, 2013). Moreover, the distinct tectonic subsidence from central Colorado to southeastern Wyoming cannot be linked to activities of basement structures (e.g., the Front Range) because the amount of tectonic subsidence does not distinctly decrease towards these structures (Figure 8). Considering the reconstructed locations of the conjugate Shatsky Rise at 80 Ma

(Figure 6), central Colorado to southeastern Wyoming were located in front of the buoyant oceanic plateau, where dynamic subsidence is predicted to be significant. The coincidence in the timing of the increased subsidence at the east of the Moxa arch and southern Utah (Figure 6) and uplifts of the Moxa arch and the Kaibab uplift suggests a possible causal relationship—flexural subsidence due to loading of these local Laramide-style uplifts (Heller & Liu, 2016; Rudolph et al., 2015). For a similar reason, the local west–east trended area of minor tectonic subsidence south of the Uinta uplift (Figure 6a,b) could be attributed to the early stage of the Uinta uplift, consistent with the timing of the Uinta uplift (ca. 75 Ma) indicated by detrital zircon provenance data (Bartschi et al., 2018; Lynds & Xie, 2019).

The uplift (or very low tectonic subsidence) in central and southwestern Wyoming can be attributed to the foredeep uplift/rebound during the quiescence phase of Absaroka thrusts (Liu et al., 2005). This regional-scale uplift is also supported by the major unconformity at the base of the Trail Member of the Ericson Formation across most of Wyoming (Liu et al., 2005; Rudolph et al., 2015). The uplift (or very low tectonic subsidence) in central and eastern Utah, however, cannot be explained by foredeep rebound because thrusts in central Utah were active (DeCelles, 2004). One possible cause of the uplift in central and eastern Utah is dynamic uplift, considering that the buoyant conjugate Shatsky Rise migrated across this area during this time (Figure 7). The uplift in central and eastern Utah may also be linked to the San Rafael Swell, the initiation age of which has been considered as early as ca. 77 Ma (Aschoff & Steel, 2011; Bartschi et al., 2018).

5.4 | Late Campanian to Maastrichtian (74.6–66 ma)

The segregated subareas of tectonic subsidence during the late Campanian to Maastrichtian strongly indicate flexural subsidence due to lithospheric loading of adjacent Laramide-style uplifts because the elongation direction of these subareas follows the orientation of adjacent Laramide-style uplifts very well (Figure 7). Still, the broad composite area of tectonic subsidence extending from north-central Colorado to eastern central Wyoming, which has also been revealed in previous studies using isopach maps (DeCelles, 2004; Jones et al., 2011; Roberts & Kirschbaum, 1995), likely reflect some degrees of dynamic subsidence. Considering the modelled location of the conjugate Shatsky Rise at 75 Ma, the dynamic subsidence in north-central Colorado to eastern central Wyoming can be linked to mantle downwelling flows in

front of the oceanic plateau (Figure 8). Another important piece of evidence suggestive of dynamic subsidence is the magnitude of tectonic subsidence in some subareas (Wind River basin, east Washakie basin) is comparable to, or even larger than the flexural subsidence in front of the Sevier fold-thrust belt over the same time duration (Figures 4 and 5). Considering the relatively local scale of Laramide-style uplifts, the abnormally large tectonic subsidence in these subareas likely reflects flexural loading of adjacent basement-involved uplifts and additional dynamic subsidence. The magnitude of dynamic subsidence can be estimated to be 300 ± 100 m based on the magnitude of 'background' tectonic subsidence in the broad area (Figure 7).

During this time, western Wyoming was located in the wedge-top zone. The Rock Springs uplift probably also contributed to the very low tectonic subsidence (<200 m) to even uplift (up to ca. 200 m) in southwestern Wyoming (Figure 7). The low tectonic subsidence and uplift in northeastern, central and southern Utah are likely resulted from some Laramide-style uplifts (e.g., Uinta uplift, San Rafael Swell and Circle Cliffs uplift). Another possible cause of the low tectonic subsidence and uplift in these areas is dynamic uplift, caused when the trailing part of the (still buoyant) oceanic plateau migrated below these areas.

6 | DISCUSSION: NEW CONSTRAINTS OF DYNAMIC TOPOGRAPHY IN THE LATE CRETACEOUS CFB

The effects (e.g., location, extent and magnitude) of dynamic topography in the CFB are better quantified through 3D flexural backstripping. The dynamic topography can be documented or inferred to have influenced the study area from 90.2 to 66 Ma based on the new tectonic subsidence maps. During the late Turonian to middle Campanian (90.2–80.2 Ma), dynamic subsidence likely influenced areas relatively close (within ca. 300 km) to the Sevier fold-thrust belt in combination with flexural subsidence generated by the Sevier fold-thrust belt to the west and possibly early activities of some basement structures (Figure 8). During the late Campanian to Maastrichtian (74.6–66 Ma), dynamic subsidence mainly influenced areas >400 km from the Sevier fold-thrust belt in combination with the flexural subsidence generated by different Laramide-style uplifts. In the following section, we focus on discussing the new constraints of dynamic topography (particularly dynamic subsidence) based on the middle to late Campanian (80.2–74.6 Ma) tectonic subsidence maps

because the effects of dynamic subsidence were not seriously interfered with other tectonic processes during this time interval.

The influence of dynamic subsidence in the CFB during the Late Cretaceous is best revealed in the middle to late Campanian (80.2–74.6 Ma) tectonic subsidence map. Although (forward) flexural modelling was not conducted here to remove the flexure generated by loading of the Sevier fold-thrust belt, the >100 m tectonic subsidence in the broad area from north-central Colorado to southeastern Wyoming during 80.2–74.6 Ma (Figures 6 and 8) can be attributed mostly to dynamic subsidence because flexural loading of the Sevier fold-thrust belt is unlikely to generate any distinct topography at >300 km away (Jordan, 1981; Liu et al., 2014; Painter & Carrapa, 2013). Thus, the area influenced by >100 m dynamic subsidence is approximately 400 by 500 km, within which significant (>200 m) dynamic subsidence occurs in a lunate-shaped subregion (ca. 450 by 150 km; area outlined in Figure 6). This subregion could be attributed to the heterogeneity in the mantle or downgoing slab or an artefact of data distribution. Still, the irregular shape of the subregion of significant (>200 m) dynamic subsidence (Figure 6b) indicates the effects of mantle-induced dynamic topography are more spatially heterogenous than previously considered, especially compared to the smoothly varying dynamic topography (in terms of magnitude) predicted by different geodynamic models for the same area and time interval.

Although the location of the dynamic subsidence in the CFB during 80.2–74.6 Ma—central Colorado to southeastern Wyoming—is generally consistent with results of previous studies based on isopach maps (Cross & Pilger, 1978; Li & Aschoff, 2022a; Painter & Carrapa, 2013), tectonic subsidence maps developed through 3D flexural backstripping indicate the area subject to strong dynamic subsidence (>200 m) is much more irregularly shaped compared to which is shown on the isopach map (Figure 3c; Li & Aschoff, 2022a). When the irregularly-shaped accommodation produced by dynamic subsidence during the middle to late Campanian was filled with sediments, the flexure caused by sediment loading would have broadened and smoothed the area of strong dynamic subsidence, thus forming a 'broader depozone' in isopach maps or total subsidence maps (Figure 3c). Thus, simply attributing the broad depocenter revealed on isopach maps to dynamic subsidence may overestimate the extent of the area subject to significant dynamic subsidence, as well as the complex effects of mantle-induced dynamic topography.

The magnitude of dynamic subsidence can be conservatively estimated to be 300 ± 100 m based on the 80.2–74.6 Ma tectonic subsidence maps (Figure 6). This number (i.e., 300 ± 100 m) is consistent with the magnitude of the

background subsidence (which is attributed to dynamic subsidence) from north-central Colorado to eastern Wyoming shown in the late Campanian to Maastrichtian (74.6–66 Ma) tectonic subsidence map (Figure 7). Based on the uplift in southern Utah during the late Turonian to middle Campanian (90.2–80.2 Ma), which is consistent with the modelled arrival of the conjugate Shatsky Rise beneath this area at ca. 80 Ma, 200–300 m appears to be a good constraint for the maximum magnitude of dynamic uplift (Figure 5). Therefore, the maximum magnitude of the gross dynamic topography in the Late Cretaceous CFB is in the range of 500–600 m.

Tectonic subsidence maps also show the rate of dynamic subsidence decreased at ca. 75 Ma. Although both 80.2–74.6 Ma and 74.6–66 Ma isopach maps reveal dynamic subsidence of similar magnitude (i.e., 300 m), the dynamic subsidence was generated over different durations. The rate of dynamic subsidence during 80.2–74.6 Ma was ca. 60 m/m.y. (Figure 6), whilst distinctly decreased to ca. 30 m/m.y. during 74.6–66 Ma (Figure 7). The decrease in the dynamic subsidence rate in north-central Colorado and eastern Wyoming rate after 74.6 Ma likely reflects an interference with dynamic uplift when the (still relatively buoyant) conjugate Shatsky Rise migrated across these areas during ca. 70 to 65 Ma (Figure 7; Dávila & Lithgow-Bertelloni, 2015). The changes in the location and rate of dynamic subsidence from 80.2 to 66 Ma reinforce the notion that the effects of dynamic topography are highly transitory (Li & Aschoff, 2022a; Liu, 2015).

Tectonic subsidence maps developed through 3D flexural backstripping can more accurately characterize the effects of dynamic topography and other tectonic processes. Although detailed isopach maps generally reveal the spatial variation in subsidence and uplift, and the approximate location of tectonic subsidence, depocenters revealed on isopach maps are usually broader than the area of tectonic subsidence (both flexural and dynamic) revealed by tectonic subsidence maps developed through 3D flexural backstripping. This is because flexure due to sediment loading will inevitably broaden and alter the original extent of tectonic subsidence. More importantly, by removing flexure caused by sediment loading, tectonic subsidence maps are also more effective in revealing areas of tectonic uplift (including dynamic uplift), which sometimes are not discernible on isopach or total subsidence maps because flexure due to sediment loading may be larger in magnitude than tectonic uplift (e.g., tectonic uplifts in southern Utah and northern Colorado during 90.2–80.2 in Figure 5 were not revealed by isopach or total subsidence maps). Therefore, isopach maps need to be used with more caution as substitutes for tectonic subsidence maps. However, it seems that as long as flexure caused by sediment loading is removed, the first-order tectonic

subsidence (and uplift) trend is generally consistent amongst conditions with different common lithospheric rigidities (Figures 4–7). The selection of lithospheric rigidity most distinctly influences the reconstructed location, extent and magnitude of maximum tectonic subsidence/uplift (Figures 4–7). Therefore, the application of the 3D flexural backstripping technique requires enough control points for high-resolution isopach and total subsidence maps and a fairly good understanding of the spatial variability in the lithospheric variability. A good understanding of the effects of dynamic topography (and the topography generated by other tectonic processes) in the CFB and other sedimentary basins is critical to refine or calibrate the mantle convection model and understand the link between deep-earth and surficial processes.

7 | CONCLUSIONS

Three-dimensional (3D) flexural backstripping in the central part of the Cordilleran Foreland Basin (CFB) was applied to the Upper Cretaceous strata to constrain the effects (e.g., location, extent and magnitude) of different subsidence mechanisms (e.g., flexural subsidence and dynamic topography). This method is different from previous backstripping efforts in the CFB because it uses the 3D flexural (versus 1D airy isostasy or 2D flexural) method in the backstripping calculations, considers overlying and underlying stratal compaction and integrates more densely spaced control points (627 total) within a well-constrained chronostratigraphic framework. The main conclusions of this study are:

1. Tectonic subsidence maps developed through 3D flexural backstripping, compared to isopach maps, can provide more stringent constraints of the effects (e.g., location, extent and magnitude) of different subsidence mechanisms (e.g., flexural subsidence and dynamic topography) in the CFB through the Late Cretaceous. Flexural subsidence caused by loading of the Sevier fold-thrust belt is the dominant subsidence mechanism in the CFB during the Cenomanian to late Turonian (100.5–90.2 Ma) and is mostly restricted to areas less than 250 km from the thrust belt (foredeep to the proximal backbulge). During the late Turonian to middle Campanian (90.2–80.2 Ma), the foredeep to proximal backbulge regions was likely subject to both flexural subsidence and dynamic subsidence because flexural subsidence generated by a topographic load alone cannot explain hundreds of meters of subsidence at the forebulge and proximal backbulge regions.
2. The middle to late Campanian (80.2–74.6 Ma) tectonic subsidence maps best reveal the extent and

magnitude of dynamic subsidence (and uplift). The area of dynamic subsidence covers an area approximately 400 by 500 km large, within which significant dynamic subsidence (>200 m) occurs in an irregular-shaped (i.e., lunate) subregion (ca. 450 by 150 km). The maximum magnitude of dynamic subsidence is 300 ± 100 m, and a good constraint for the maximum magnitude of dynamic uplift is 200–300 m. Therefore, the net topography generated by mantle-induced dynamic topography in the Late Cretaceous CFB is ca. 500–600 m. The decrease in dynamic subsidence rate from 60 to 30 m/m.y. after 75 Ma is likely due to dynamic uplift, which can be linked to the (still relatively buoyant) conjugate Shatsky Rise as it is modelled to have migrated from north-central Colorado to eastern Wyoming.
3. The application of 3D flexural backstripping requires a large enough number of control points for isopach and total subsidence maps and a fairly good understanding of the spatial variability in lithospheric rigidities. Tectonic subsidence maps developed through 3D flexural backstripping are more capable of revealing the spatial heterogeneity in the effects of dynamic topography. The more quantitative constraints of the effects of dynamic topography provided by the application of 3D flexural backstripping in sedimentary basins worldwide can help advance the current geodynamic model of mantle flows and our understanding of the link between deep-earth and surficial processes.

PEER REVIEW
The peer review history for this article is available at https://publons.com/publon/10.1111/bre.12706.

DATA AVAILABILITY STATEMENT
The data that support the findings of this study are available from the corresponding author upon reasonable request.

ORCID
Zhiyang Li https://orcid.org/0000-0002-2908-4098

REFERENCES

Allen, P. A., & Allen, J. R. (2013). *Basin analysis: Principles and application to petroleum play assessment*. Wiley-Blackwell.

Angevine, C. L., Heller, P. L., & Paola, C. (1990). Quantitative sedimentary basin modeling. *American Association of Petroleum Geologists Short Course*, *32*, 247.

Aschoff, J., & Steel, R. (2011). Anomalous clastic wedge development during the Sevier-Laramide transition, north American cordilleran Foreland Basin, USA. *GSA Bulletin*, *123*, 1822–1835. https://doi.org/10.1130/B30248.1

Bartschi, N. C., Saylor, J. E., Lapen, T. J., Blum, M. D., Pettit, B. S., & Andrea, R. A. (2018). Tectonic controls on late cretaceous sediment provenance and stratigraphic architecture in the book cliffs, Utah. *GSA Bulletin*, *130*, 1763–1781. https://doi.org/10.1130/B31927.1

Beaumont, C. (1981). Foreland basins. *Geophysical Journal International*, *65*, 291–329.

Bechtel, T. D., Forsyth, D. W., Sharpton, V. L., & Grieve, R. A. F. (1990). Variations in effective elastic thickness of the north American lithosphere. *Nature*, *343*, 636–638. https://doi.org/10.1038/343636a0

Bond, G. (1976). Evidence for continental subsidence in North America during the late cretaceous global submergence. *Geology*, *4*, 557–560. https://doi.org/10.1130/0091-7613(1976)4<557:EFCSIN>2.0.CO;2

Burgess, P. M., Gurnis, M., & Moresi, L. (1997). Formation of sequences in the Cratonic interior of North America by interaction between mantle, eustatic, and stratigraphic processes. *GSA Bulletin*, *109*, 1515–1535. https://doi.org/10.1130/0016-7606(1997)109<1515:FOSITC>2.3.CO;2

Burgess, P. M., & Moresi, L. (1999). Modelling rates and distribution of subsidence due to dynamic topography over subducting slabs: Is it possible to identify dynamic topography from ancient strata? *Basin Research*, *11*, 305–314. https://doi.org/10.1046/j.1365-2117.1999.00102.x

Catuneanu, O., Beaumont, C., & Waschbusch, P. (1997). Interplay of static loads and subduction dynamics in foreland basins: Reciprocal stratigraphies and the "missing" peripheral bulge. *Geology*, *25*, 1087–1090. https://doi.org/10.1130/0091-7613(1997)025<1087:IOSLAS>2.3.CO;2

Chang, C., & Liu, L. (2019). Distinct responses of intraplate sedimentation to different subsidence mechanisms: Insights from forward landscape evolution simulations. *Journal of Geophysical Research: Earth Surface*, *124*, 1139–1159. https://doi.org/10.1029/2018JF004905

Chang, C., & Liu, L. (2020). Investigating the formation of the cretaceous Western interior seaway using landscape evolution simulations. *GSA Bulletin*, *133*, 347–361. https://doi.org/10.1130/B35653.1

Colleoni, F., De Santis, L., Pochini, E., Forlin, E., Geletti, R., Brancatelli, G., Tesauro, M., Busetti, M., & Braitenberg, C. (2021). Paleostripv1.0 - A user-friendly 3d backtracking software to reconstruct paleo-bathymetries. *Geoscientific Model Development Discussion*, *2021*, 1–33. https://doi.org/10.5194/gmd-2021-78

Cross, T. A., & Pilger, R. H. (1978). Tectonic controls of late cretaceous sedimentation, Western interior, USA. *Nature*, *274*, 653–657. https://doi.org/10.1038/274653a0

Dávila, F. M., & Lithgow-Bertelloni, C. (2015). Dynamic uplift during slab flattening. *Earth and Planetary Science Letters*, *425*, 34–43. https://doi.org/10.1016/j.epsl.2015.05.026

DeCelles, P. G., & Giles, K. A. (1996). Foreland Basin systems. *Basin Research*, *8*, 105–123. https://doi.org/10.1046/j.1365-2117.1996.01491.x

DeCelles, P. G. (2004). Late Jurassic to Eocene evolution of the cordilleran Thrust Belt and Foreland Basin system, Western U.S.A. *American Journal of Science*, *304*, 105–168. https://doi.org/10.2475/ajs.304.2.105

DeCelles, P. G. (2012). Foreland Basin systems revisited: Variations in response to tectonic settings. In C. Busby & A. Azor (Eds.), *Tectonics of sedimentary basins* (pp. 405–426). John Wiley & Sons. https://doi.org/10.1111/j.1365-2117.1992.tb00146.x

Dickinson, W. R., Klute, M. A., Hayes, M. J., Janecke, S. U., Lundin, E. R., McKittrick, M. A., & Olivares, M. D. (1988). Paleogeographic and paleotectonic setting of Laramide sedimentary basins in the central Rocky Mountain region. *GSA Bulletin*, *100*, 1023–1039. https://doi.org/10.1130/0016-7606(1988)100<1023:PAPSOL>2.3.CO;2

Flament, N., Gurnis, M., & Müller, R. D. (2013). A review of observations and models of dynamic topography. *Lithosphere*, *5*, 189–210. https://doi.org/10.1130/L245.1

Gurnis, M. (1992). Rapid continental subsidence following the initiation and evolution of subduction. *Science*, *255*, 1556–1558. https://doi.org/10.1126/science.255.5051.1556

Haque, Z., Geissman, J. W., DeCelles, P. G., & Carrapa, B. (2020). A magnetostratigraphic age constraint for the proximal Synorogenic conglomerates of the late cretaceous cordilleran Foreland Basin, Northeast Utah, USA. *GSA Bulletin*, *133*, 1795–1814. https://doi.org/10.1130/B35768.1

Heller, P. L., Bowdler, S. S., Chambers, H. P., Coogan, J. C., Hagen, E. S., Shuster, M. W., Winslow, N. S., & Lawton, T. F. (1986). Time of initial thrusting in the Sevier Orogenic Belt, Idaho-Wyoming and Utah. *Geology*, *14*, 388–391. https://doi.org/10.1130/0091-7613(1986)14<388:TOITIT>2.0.CO;2

Heller, P. L., Angevine, C. L., Winslow, N. S., & Paola, C. (1988). Two-phase stratigraphic model of Foreland-Basin sequences. *Geology*, *16*, 501–504. https://doi.org/10.1130/0091-7613(1988)016<0501:tpsmof>2.3.co;2

Heller, P. L., & Liu, L. (2016). Dynamic topography and vertical motion of the U.S. Rocky Mountain region prior to and during the Laramide orogeny. *GSA Bulletin*, *128*, 973–988. https://doi.org/10.1130/B31431.1

Humphreys, E. D., Schmandt, B., Bezada, M. J., & Perry-Houts, J. (2015). Recent craton growth by slab stacking beneath Wyoming. *Earth and Planetary Science Letters*, *429*, 170–180. https://doi.org/10.1016/j.epsl.2015.07.066

Jones, C. H., Farmer, G. L., Sageman, B., & Zhong, S. (2011). Hydrodynamic mechanism for the Laramide orogeny. *Geosphere*, *7*, 183–201. https://doi.org/10.1130/GES00575.1

Jordan, T. E. (1981). Thrust loads and Foreland Basin evolution, cretaceous, Western United States. *AAPG Bulletin*, *65*, 2506–2520. https://doi.org/10.1306/03B599F4-16D1-11D7-8645000102C1865D

Kauffman, E. G. (1977). Geological and biological overview: Western interior cretaceous basin. *Mountain Geologist*, *14*, 75–99.

Kauffman, E. G. (1985). Cretaceous evolution of the Western Interior Basin of the United States. *SEPM Guidebook*, *4*, iv–xiii.

Kauffman, E. G., & Caldwell, W. G. E. (1993). The Western Interior Basin in space and time. *Special Paper - Geological Association of Canada*, *39*, 1–30.

Kominz, M. A., Browning, J. V., Miller, K. G., Sugarman, P. J., Mizintseva, S., & Scotese, C. R. (2008). Late Cretaceous to

Miocene sea-level estimates from the New Jersey and Delaware coastal plain coreholes: An error analysis. *Basin Research*, *20*, 211–226. https://doi.org/10.1111/j.1365-2117.2008.00354.x

Koppers, A. A. P., Becker, T. W., Jackson, M. G., Konrad, K., Müller, R. D., Romanowicz, B., Steinberger, B., & Whittaker, J. M. (2021). Mantle plumes and their role in earth processes. *Nature Reviews Earth & Environment*, *2*, 382–401. https://doi.org/10.1038/s43017-021-00168-6

Laskowski, A. K., DeCelles, P. G., & Gehrels, G. E. (2013). Detrital zircon geochronology of cordilleran Retroarc Foreland Basin strata, Western North America. *Tectonics*, *32*, 1027–1048. https://doi.org/10.1002/tect.20065

Lawton, T. F. (2008). Chapter 12 Laramide sedimentary basins. In A. D. Miall (Ed.), *Sedimentary basins of the world* (Vol. *5*, pp. 429–450). Elsevier.

Lazauskien, J., Stephenson, R., Šliaupa, S., & van Wees, J.-D. (2002). 3-D flexural modelling of the Silurian Baltic Basin. *Tectonophysics*, *346*, 115–135. https://doi.org/10.1016/S0040-1951(01)00231-1

Leary, R., DeCelles, P., Gehrels, G., & Morriss, M. (2015). Fluvial deposition during transition from flexural to dynamic subsidence in the cordilleran Foreland Basin: Ericson formation, Western Wyoming, USA. *Basin Research*, *27*, 495–516. https://doi.org/10.1111/bre.12085

Li, Z., & Aschoff, J. (2022a). Constraining the effects of dynamic topography on the development of late cretaceous cordilleran Foreland Basin, Western United States. *GSA Bulletin*, *134*, 446–462. https://doi.org/10.1130/B35838.1

Li, Z., & Aschoff, J. (2022b). Shoreline evolution in the late cretaceous north American cordilleran Foreland Basin: An exemplar of the combined influence of tectonics, sea level, and sediment supply through time. *Earth-Science Reviews*, *226*, 103947. https://doi.org/10.1016/j.earscirev.2022.103947

Liu, L., Spasojević, S., & Gurnis, M. (2008). Reconstructing Farallon plate subduction beneath North America Back to the late cretaceous. *Science*, *322*, 934–938. https://doi.org/10.1126/science.1162921

Liu, L., & Gurnis, M. (2010). Dynamic subsidence and uplift of the Colorado plateau. *Geology*, *38*, 663–666. https://doi.org/10.1130/G30624.1

Liu, L. (2015). The ups and downs of North America: Evaluating the role of mantle dynamic topography since the Mesozoic. *Reviews of Geophysics*, *53*, 1022–1049. https://doi.org/10.1002/2015RG000489

Liu, S., & Nummedal, D. (2004). Late cretaceous subsidence in Wyoming: Quantifying the dynamic component. *Geology*, *32*, 397–400. https://doi.org/10.1130/G20318.1

Liu, S., Nummedal, D., Yin, P., & Luo, H. (2005). Linkage of Sevier thrusting episodes and late cretaceous Foreland Basin Megasequences across southern Wyoming (USA). *Basin Research*, *17*, 487–506. https://doi.org/10.1111/j.1365-2117.2005.00277.x

Liu, S., Nummedal, D., & Liu, L. (2011). Migration of dynamic subsidence across the late cretaceous United States Western Interior Basin in response to Farallon plate subduction. *Geology*, *39*, 555–558. https://doi.org/10.1130/G31692.1

Liu, S., Nummedal, D., & Gurnis, M. (2014). Dynamic versus flexural controls of late cretaceous Western Interior Basin, USA. *Earth and Planetary Science Letters*, *389*, 221–229. https://doi.org/10.1016/j.epsl.2014.01.006

Liu, S., & Currie, C. A. (2016). Farallon plate dynamics prior to the Laramide orogeny: Numerical models of flat subduction. *Tectonophysics*, *666*, 33–47. https://doi.org/10.1016/j.tecto.2015.10.010

Liu, L., Gurnis, M., Seton, M., Saleeby, J., Müller, R. D., & Jackson, J. M. (2010). The role of oceanic plateau subduction in the Laramide orogeny. *Nature Geoscience*, *3*, 353–357. https://doi.org/10.1038/ngeo829

Livaccari, R. F., Burke, K., & Şengör, A. M. C. (1981). Was the Laramide orogeny related to subduction of an oceanic plateau? *Nature*, *289*, 276–278. https://doi.org/10.1038/289276a0

Livaccari, R. F. (1991). Role of crustal thickening and extensional collapse in the tectonic evolution of the Sevier-Laramide orogeny, Western United States. *Geology*, *19*, 1104–1107. https://doi.org/10.1130/0091-7613(1991)019<1104:ROCTAE>2.3.CO;2

Luo, H., & Nummedal, D. (2012). Forebulge migration: A three-dimensional flexural numerical modeling and subsurface study of southwestern Wyoming. In D. Gao (Ed.), *Tectonics and sedimentation: Implications for petroleum systems: AAPG Memoir* (pp. 377–395). The American Association of Petroleum Geologists.

Lynds, R. M., & Xie, X. (2019). Detrital zircon geochronology of upper cretaceous to Paleocene sandstones from south-Central Wyoming: Evidence for middle Campanian Laramide deformation. *Tectonics*, *38*, 4077–4098. https://doi.org/10.1029/2019TC005636

Marshak, S., Domrois, S., Abert, C., Larson, T., Pavlis, G., Hamburger, M., Yang, X., Gilbert, H., & Chen, C. (2017). The basement revealed: Tectonic insight from a digital elevation model of the great unconformity, USA Cratonic platform. *Geology*, *45*, 391–394. https://doi.org/10.1130/G38875.1

Martinson, V. S., Heller, P. L., & Frerichs, W. E. (1998). Distinguishing middle late cretaceous tectonic events from Regional Sea-level change using foraminiferal data from the U.S. Western Interior. *GSA Bulletin*, *110*, 259–268. https://doi.org/10.1130/0016-7606(1998)110<0259:DMLCTE>2.3.CO;2

Miller, K. G., Kominz, M. A., Browning, J. V., Wright, J. D., Mountain, G. S., Katz, M. E., Sugarman, P. J., Cramer, B. S., Christie-Blick, N., & Pekar, S. F. (2005). The phanerozoic record of global sea-level change. *Science*, *310*, 1293–1298. https://doi.org/10.1126/science.1116412

Mitrovica, J. X., Beaumont, C., & Jarvis, G. T. (1989). Tilting of continental interiors by the dynamical effects of subduction. *Tectonics*, *8*, 1079–1094. https://doi.org/10.1029/TC008i005p01079

Morris, M., Fernandes, V. M., & Roberts, G. G. (2020). Extricating dynamic topography from subsidence patterns: Examples from eastern North America's passive margin. *Earth and Planetary Science Letters*, *530*, 115840. https://doi.org/10.1016/j.epsl.2019.115840

Moucha, R., Forte, A. M., Mitrovica, J. X., Rowley, D. B., Quéré, S., Simmons, N. A., & Grand, S. P. (2008). Dynamic topography and long-Term Sea-level variations: There is no such thing as a stable continental platform. *Earth and Planetary Science Letters*, *271*, 101–108. https://doi.org/10.1016/j.epsl.2008.03.056

Painter, C. S., & Carrapa, B. (2013). Flexural versus dynamic processes of subsidence in the north American cordillera Foreland Basin. *Geophysical Research Letters*, *40*, 4249–4253. https://doi.org/10.1002/grl.50831

Pang, M. (1995) *Tectonic subsidence of the cretaceous Western Interior Basin, United States* (Ph.D. Thesis). Louisiana State University.

Pang, M., & Nummedal, D. (1995). Flexural subsidence and basement tectonics of the cretaceous Western Interior

Basin, United States. *Geology*, 23, 173–176. https://doi.org/10.1130/0091-7613(1995)023<0173:FSABTO>2.3.CO;2

Richards, M. A., & Hager, B. H. (1984). Geoid anomalies in a dynamic earth. *Journal of Geophysical Research: Solid Earth*, 89, 5987–6002. https://doi.org/10.1029/JB089iB07p05987

Roberts, L. N. R., & Kirschbaum, M. A. (1995). Paleogeography and the Late Cretaceous of the Western Interior of Middle North America; Coal Distribution and Sediment Accumulation. *Professional Paper 1561*, 115 p.

Rudolph, K. W., Devlin, W. J., & Crabaugh, J. P. (2015). Upper cretaceous sequence stratigraphy of the Rock Springs uplift, Wyoming. *The Mountain Geologist*, 52, 13–157.

Sageman, B. B., & Arthur, M. A. (1994). Early Turonian paleogeographic/Paleobathymetric map, Western interior, us. In M. V. Caputo, J. A. Peterson, & K. J. Franczyk (Eds.), *Mesozoic systems of the Rocky Mountain Region, USA* (pp. 457–470). SEPM Rocky Mountain Section.

Saleeby, J. (2003). Segmentation of the Laramide slab—Evidence from the southern Sierra Nevada region. *GSA Bulletin*, 115, 655–668. https://doi.org/10.1130/0016-7606(2003)115<0655:SOTLSF>2.0.CO;2

Saylor, J. E., Rudolph, K. W., Sundell, K. E., & van Wijk, J. (2020). Laramide orogenesis driven by late cretaceous weakening of the north American lithosphere. *Journal of Geophysical Research: Solid Earth*, 125, e2020JB019570. https://doi.org/10.1029/2020JB019570

Sclater, J. G., & Christie, P. A. F. (1980). Continental stretching: An explanation of the post-mid-cretaceous subsidence of the Central North Sea Basin. *Journal of Geophysical Research: Solid Earth*, 85, 3711–3739. https://doi.org/10.1029/JB085iB07p03711

Shephard, G. E., Müller, R. D., Liu, L., & Gurnis, M. (2010). Miocene drainage reversal of the Amazon River driven by plate–mantle interaction. *Nature Geoscience*, 3, 870–875. https://doi.org/10.1038/ngeo1017 https://www.nature.com/articles/ngeo1017#supplementary-information

Spasojevic, S., Liu, L., & Gurnis, M. (2009). Adjoint models of mantle convection with seismic, plate motion, and stratigraphic constraints: North America since the late cretaceous. *Geochemistry, Geophysics, Geosystems*, 10, 1–24. https://doi.org/10.1029/2008GC002345

Steckler, M. S., & Watts, A. B. (1978). Subsidence of the Atlantic-type continental margin off New York. *Earth and Planetary Science Letters*, 41, 1–13. https://doi.org/10.1016/0012-821X(78)90036-5

Tesauro, M., Kaban, M. K., & Mooney, W. D. (2015). Variations of the lithospheric strength and elastic thickness in North America. *Geochemistry, Geophysics, Geosystems*, 16, 2197–2220. https://doi.org/10.1002/2015GC005937

Tufano, B. C., & Pietras, J. T. (2017). Coupled flexural-dynamic subsidence modeling approach for retro-foreland basins: Example from the Western Canada Sedimentary Basin. *GSA Bulletin*, 129, 1622–1635. https://doi.org/10.1130/B31646.1

Turcotte, D. L., & Schubert, G. (2002). *Geodynamics* (2nd ed.). Cambridge University Press.

Watts, A. B. (2001). *Isostasy and flexure of the lithosphere*. Cambridge University Press.

Weimer, R. J. (1984). Relation of unconformities, tectonics, and sea-level changes, cretaceous of Western interior, USA. In J. S. Sehlee (Ed.), *Interregional unconformities and hydrocarbon accumulation* (Vol. 36, pp. 7–35). American Association of Petroleum Geologists Memoir.

White, T., Furlong, K., & Arthur, M. (2002). Forebulge migration in the cretaceous Western Interior Basin of the Central United States. *Basin Research*, 14, 43–54. https://doi.org/10.1046/j.1365-2117.2002.00165.x

Wickert, A. D. (2016). Open-source modular solutions for flexural isostasy: Gflex V1.0. *Geoscientific Model Development*, 9, 997–1017. https://doi.org/10.5194/gmd-9-997-2016

Yonkee, W. A., & Weil, A. B. (2015). Tectonic evolution of the Sevier and Laramide belts within the north American cordillera orogenic system. *Earth-Science Reviews*, 150, 531–593. https://doi.org/10.1016/j.earscirev.2015.08.001

SUPPORTING INFORMATION

Additional supporting information can be found online in the Supporting Information section at the end of this article.